ANALYSIS AND VISUALIZATION OF EEG EVENT-INDUCED DYNAMIC SYNCHRONIZATION PATTERNS IN COGNITIVE TASKS

Francisco A. Alba, José L. Marroquin, Joaquin Peña and Thalia Harmony

Comunicación Técnica No I-06-05/08-03-2006
(CC/CIMAT)

Analysis and Visualization of EEG Event-Induced Dynamic Synchronization Patterns in Cognitive Tasks

Francisco A. Alba[1], Jose L. Marroquin[1], Joaquin Peña[1], Thalia Harmony[2]

[1]*Centro de Investigacion en Matematicas, Guanajuato, Mexico*
[2]*Instituto de Neurobiologia, UNAM Campus Juriquilla, Queretaro, Mexico*

Introduction

The execution of even simple cognitive tasks is characterized by the cooperation of different neural networks that are distributed across the brain, and whose synchronized activity generates oscillations of specific frequencies in the EEG [Kirschfeld, 2005]. Thus, in response to specific stimulae, one may observe not only "evoked" activity (exactly time locked to the stimulus), but also "induced" activities [Pfurtscheller and Lopes da Silva, 1999] which cannot be extracted by simple averaging, but which represent events that are localized not only spatially, but also in specific regions of the Time-Frequency (TF) plane. These events may be correlated with relative changes in power with respect of to the pre-stimulus condition (possibly due to changes in the synchronization of the underlying local neural populations [Pfurtscheller, 1977, 1992]), and therefore, may be characterized by specific activation patterns, which are located in particular regions of the TF plane, and which may be associated with specific cognitive sub-processes [Marroquin et.al., 2004; Harmony et al., 2001].

There is, however, another important characteristic of these events, which cannot be measured directly by relative power changes: the formation of dynamic global assemblies, which according to the definition by Varela et al. (2001), are "distributed local networks of neurons transiently linked by reciprocal dynamic (possibly long range) connections". It is generally accepted that these connections are correlated with the synchronization of the corresponding EEG signals in particular regions of the TF plane [Varela et al., 2001; Lopes da Silva, 1991; Singer, 1993]. Also, simulations performed with neural mass models show that a bidirectional coupling of two remote cortical areas is reflected as phase synchronization of MEG/EEG oscillations [David and Friston, 2003], which supports the idea that EEG synchrony is highly related to physiological connectivity in the cortex and thus can be used as a measure for long-range interaction.

For these reasons, there have been a number of studies of long range synchronization of EEG signals [Bressler et al., 1995; Friston et al., 1997; Lachaux et al., 1999, 2000; Rodriguez et al., 1999]. Most of these studies, however, have some limitations: one one hand, the high dimensionality of the synchrony data implies a visualization problem. Most works on the field avoid this problem by averaging across a large time window [Quian Quiroga et. al, 2002; David

and Friston, 2004; Mizuhara et. al, in press] and/or by limiting the analysis to specific frequency bands [Lachaux et. al, 1999; Rodriguez et. al, 1999]. This is far from ideal since many synchronization patterns appear only in small regions of the TF plane and one cannot obtain, from these results, a complete overall picture of the synchronization dynamics across different frequencies, which may correspond to specific cognitive sub-processes. A second problem is related to inaccuracies in the determinadion of long-range phase synchronization. These are due to two causes: The first is the volume conductor effect, which smears the effect of cortical current soures, as a result of which spurious synchronization (especially between neighboring electrodes) may appear. It has been proposed to compute the surface Laplacian of the potentials and use these signals instead of the crude potential data to estimate phase synchronization. However, as we show later, this transformation is not the most appropiate since it makes phase estimations more vulnerable to noise. The second cause is related to the local phase estimation for low frequencies using quadature filter banks (ie.- Gabor wavelets or windowed Fourier transforms): if the frequency response of a particular filter straddles the origin, the corresponding local phase will be distorted.

A final problem is related to the way in which significant synchronization changes (with respect to the pre-stimulus condition) are detected. These significant changes must be characterized by a persistent relative phase locking (or phase scattering) between the signals that correspond to each pair of electrode locations; in other words, to estimate the degree of EEG synchronization one must determine the significance of a phase-locking measure and its consistency across a given time window. The most widely used synchrony measures, such as statistical coherence and the *single trial phase-locking statistic* (STPLS) which is based on the circular variance of the phase difference [Lachaux et al., 2000], attempt to measure this indirectly, by computing the dispersion change of the corresponding phase difference over a given time window. The problem with this approach is that, as will be shown later, this measure is strongly affected by local phase dispersion changes occurring in either one of the 2 signals, which seriously interferes with the detection of true synchronization or de-synchronization events.

The purpose of this work is to present a methodology that overcomes these limitations; the main idea is to treat persistence and phase locking separately: persistence is handled via Bayesian estimation of a hidden Markov random field (MRF) that models a label field in TF space that classifies the interactions between signal pairs as significantly higher, lower or equal to the corresponding pre-stimulus average value. We also present a visualization method that permits one to perform, based on this classification, an interactive segmentation of the TF plane in terms of persistent, global Synchronization Patterns (SP's), which may be correlated with concurrent cognitive processes whose expression is multiplexed at different frequencies. Finally, the inaccuracies in the determination of the local phase are reduced by using a cortical projection method that mostly eliminates the volume conductor effect, and by carefully designing the filter bank that performs the time-frequency decomposition of the transformed data. The effectiveness of these techniques is illustrated with the analysis of

SP's associated with a figure classification task.

Materials and methods

We have tested our procedure on data from a figure classification experiment [Harmony et al., 2001] where white-line figures on a black background were presented to each subject. The subjects were instructed to press a button if the figure corresponded to an animal whose name started with a consonant, and another button if the figure did not correspond to an animal and the name of the figure started with a consonant. If the name started with a vowel, the subject was instructed not to respond. The subjects were 18 normal children (8 to 10 years old, 9 females), all right handed with normal neurological examination. The EEG signals were recorded with reference to linked ears from the sites Fp1, Fp2, F3, F4, C3, C4, P3, P4, O1, O2, F7, F8, T3, T4, T5, T6, Fz, Cz, Pz, and Oz of the 10/20 system. Sampling was done every 5 ms during a time segment from 1280 ms before the stimulus and 1500 ms after its onset. Each trial was visually edited and only those corresponding to correct responses and with no artifacts were analyzed.

Methodolody

In general, measuring EEG synchrony involves the following steps: preprocessing the raw EEG signals to handle volume conduction and reference electrode issues, estimating a time-frequency decomposition of the preprocessed signals, estimating a synchronization measure from the filtered signals for all or some electrode pairs, and visualizing the results. Particularly, we follow the following procedure:

1. Estimate virtual source (VS) signals from EEG potentials to reduce volume conduction effects.
2. Run the VS signals through a bank of bandpass quadrature filters and extract phase information (TF phase analysis).
3. Calculate the instantaneous phase-lock from the filtered VS signals.
4. Estimate the likelihoods and prior distributions for the MRF model using the instantaneous phase-lock values.
5. Use Bayesian estimation to find significant synchronization patterns that are persistent.
6. Display synchronization patterns as multitoposcopic graphs and time-frequency-topography (TFT) maps that can be interactively segmented.

We will now describe these steps in detail.

Virtual source estimation

EEG signals are given as a set of discrete voltage signals $V_{j,e}(t)$, where j is the trial number and e represents an electrode site. These voltages are measured with respect to a reference electrode which is placed in the subject's body as far as possible from any sources of electrical activity; some common choices are the chin, or linked ears. However, electric activity in the reference electrode is not null and affects all EEG measures. On the other hand, we have the issue of the volume conductor [Nunez, 1995] which smears the potentials across the surface. These two problems may lead to unreliable results, especially when measuring synchrony.

To correct for the reference effect, one possible solution is to substract the "average electrode" signal, computed as the average of all lead signals for each time [Hagemann et al., 2001; Hoechstetter et al., 2004]. This effectively removes the reference, but introduces a new bias $\bar{V} = (1/N_e)\sum_e V_e$ (where V_e are the true reference-free signals). In the case of event-induced synchrony analysis, this new bias ay have a stronger distorting effect because, unlike $R(t)$, it may be correlated among trials, and it may also be correlated with the stimulus presentation, as is clearly the case with evoked potentials.

We have analyzed this effect using synthetic signals, and found that in fact the bias introduced by $\bar{V}$ may have a strong effect in the detection of event-induced synchrony, introducing spurious synchronization patterns and masking significant synchrony events, whereas R does not produce these effects (provided that its magnitude is relatively small). The synthetic reference-free signals V_e are given by

$$V_e(t) = \alpha_e \cos(\omega t + \phi_1) + (1 - \alpha_e)\cos(\omega t + \phi_2) + \eta_e(t),\ \eta_e(t) \sim \mathcal{N}(0, \sigma_\eta), \quad (1)$$

for each recording site e. These signals are based on a population model described later in this paper. Careful choice of the σ_e parameters allows one to model amplitude and synchronization changes (provided that $\phi_1 \neq \phi_2$ - see Figure 12). We may model a global decrease in phase-lock (between all electrode pairs) by increasing the variance of the α_e's with respect to the baseline. Furthermore, the observed signals V^* may be modeled as

$$V_e^*(t) = V_e(t) + R(t), \quad (2)$$

where $R(t)$ is the reference effect signal. For this example, $R(t)$ was modeled as low-frequency noise by passing white (uniform) noise through a bandpass Gabor filter centered at 2 Hz with a bandwidth of 2 Hz. The amplitue of R is about one tenth of the amplitude of V_e.

We performed our synchrony analysis (described below) using the reference-free signals V, the observed signals V^*, and the average reference (AR) signals $V^* - \bar{V}^*$. The results using both the reference-free and observed signals show, as expected, a decrease of synchrony for each electrode pair. The AR signals, however, show significative phase-lock increments in some regions, possibly introduced by the bias described above. For this reason, we do not use the average reference in our method.

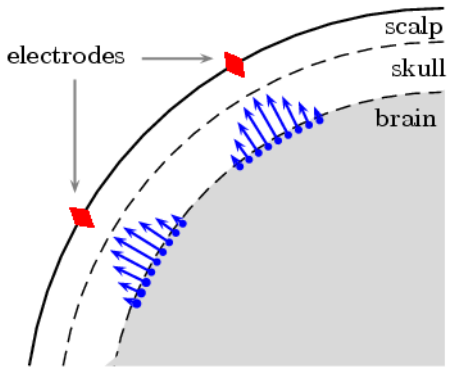

Figure 1: Distribution of equivalent radial dipole groups (virtual sources) located near the brain surface.

On the other hand there is the issue of volume conduction. Different techniques have been used to avoid this problem and increase the EEG spatial resolution. Two of them are solving the inverse problem [David et al., 2001], and estimating the surface Laplacian of the potential (known in the literature as current source density or CSD). When performing amplitude or spectral analysis, the latter method is preferred since the current source density (CSD) is not sensitive to the reference potential and effectively diminishes the volume conductor effects [Pascual-Marqui et al., 1988; Perrin et al., 1989]. Moreover, recent works have already used CSD instead of potentials to measure long-range synchronization based on phase-lock measurings [Mizuhara et al., 2005]; however, our tests have shown that this is not the best choice. The complex surface Laplacian may be approximated by the resultant of the vectors that represent the quadrature filter outputs in the complex plane: since the measured potentials are in fact very smooth functions of the spatial position, partly because of volume conduction effects, the surface Laplacian of the complex output of a quadrature filter at any time point will have very small magnitude, which makes the estimated phase (i.e.- the angle of the vector representing this number in the complex plane) very sensitive to noise and to the precise interpolation method used. For this reason, we propose to use instead the phase of virtual current sources, which we assume are located in the cortex, directly below the actual electrodes. To compute these signals, one has to solve the corresponding inverse problem; to make this problem well-posed, we make the assumption that below each electrode site there is a population of radial sources whose strength decreases exponentially with the distance to the electrode (see Figure 1). It is worth noting that a similar approach has been proposed in [Hoechstetter et al., 2004] where virtual sources (dipoles) are placed in cortical regions of interest (which can be obtained from averaged evoked data) and in regions of possible background activity.

From the quasi-static approximation of Maxwell's equations in linear isotropic

media, the relationship between the potential recordings and the sources is given by $\Phi = KJ$ [Malmivuo and Plonsey, 1995], where Φ is a n-vector of instantaneous electrical recordings, J is a vector of dipole components, and K is the lead field matrix.

We group equivalent dipoles in n sets formed by p radial dipoles, $\{\alpha_1 j_{s_1}, \ldots, \alpha_p j_{s_p}\}$, with $||j_{s_r}|| = 1$ and $0 < \alpha_r \leq 1$, so that we can express $J = (w_1 J_1^t, \ldots, w_n J_n^t)$, where w_s is a scalar factor and $J_s = (\alpha_1 j_{s_1}^t, \ldots, \alpha_p j_{s_p}^t)^t$. Note that weights $\alpha_1, \ldots, \alpha_p$ have the same values in each group (assuming all electrodes to be equally sensitive), thus each factor w_s represents the strength of the s-th dipole group. If $K = [K_1, \ldots, K_n]$, with K_s the lead field matrix associated to the s-th group, then

$$\Phi = KJ = \sum_{s=1}^{n} (K_s J_s) w_s = Gw \tag{3}$$

where G is the $n \times n$ matrix $[K_1 J_1, \ldots, K_n J_n]$, and $w = (w_1, \ldots, w_n)^t$.

The lead field matrix K is computed using a three-concentric-spheres inhomogeneous head model [Zhang, 1995], and the resulting matrix G is well-conditioned. Therefore, given the potentials Φ we may obtain the strengths w by

$$w = G^{-1}\Phi. \tag{4}$$

The virtual source strengths $w_e(t)$ provide better spatial localization than potentials but with a magnitude large enough to yield reliable phase estimations. Figure 2 shows the resulting synchrony patterns obtained with our procedure (described below) for synthetic signals using raw potentials (left graph) and the estimated VS signals (right graph). The signals were obtained by placing one dipole near F3 and another between P4 and T6 of the 10/20 system. Noise was added to all electrode readings. The dipoles are unsynchronized (out of phase) in the pre-stimulus segment (not shown) and in perfect synchrony in the post-stimulus. The graphs show significant increment (red) or decrement (green) in synchrony for all electrode pairs.

Time-Frequency Phase Analysis

To obtain a time-frequency decomposition of the EEG signals, it is common to resort to the short-time FFT or quadrature bandpass filters. We have chosen to work with quadrature filters, which are easy to implement and may be tuned to any frequency (not only Fourier discrete frequencies). A quadrature filter can be defined as one whose frequency response is zero for negative frequencies. One common example of quadrature filters are Gabor filters, which have a Gaussian frequency response, but when implemented digitally the response is truncated to a certain range (4σ around the center frequency is a common choice). When these filters ae tuned at low frequencies, however, they present the problem of having a large response at negative frequencies, which severly distorts the phase estimates (see Figure 3).

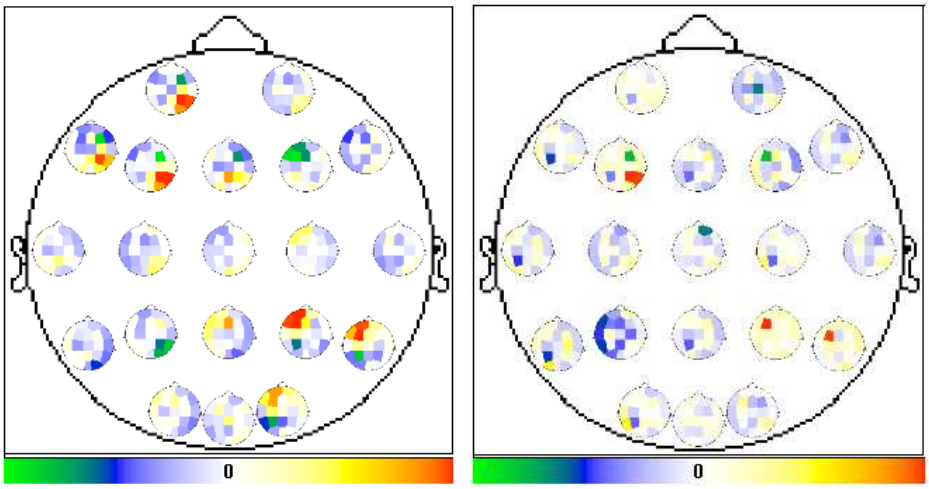

Figure 2: Synchrony patterns obtained from synthetic data using raw potentials (left image) and the estimated virtual source signals (right image).

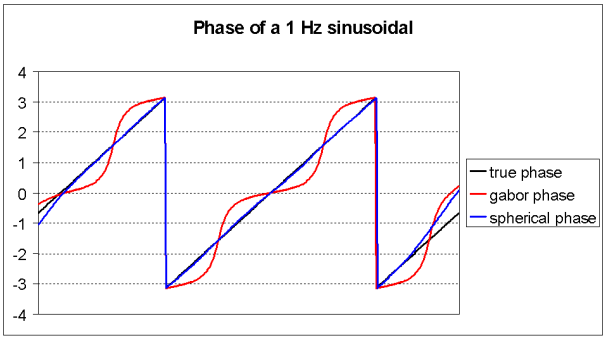

Figure 3: True phase and estimated phase (using Gabor and spherical quadrature filters) for a 1 Hz sinusoidal signal.

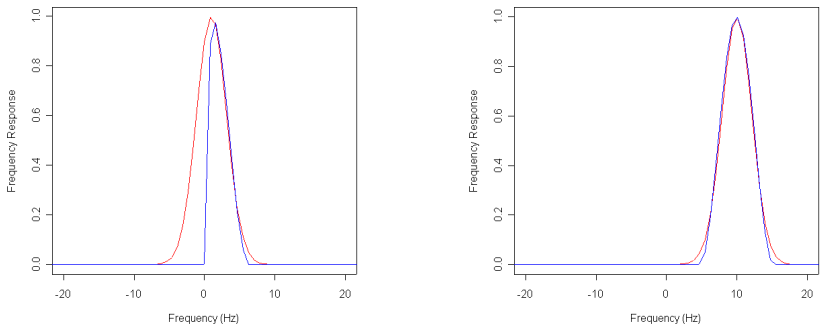

Figure 4: Bandpass filters centered at 1 Hz (left) and 10 Hz (right). The red curve shows the frequency response of a Gabor filter, while the blue curve shows the response of a spherical filter.

In our procedure, we run the VS signals through a bank of band-pass spherical quadrature filters [Guerrero, 2005] centered at intervals of 1 Hz and with a bandwidth of about 2 Hz each. These filters have the following frequency response:

$$G_{\omega_k,h}(\omega) = \begin{cases} \frac{1}{2}\left[1+\sin\left(\frac{(h_k+2(\omega-\omega_k))\pi}{2h_k}\right)\right] & \text{if } \omega \in [\omega_k - h_k, \omega_k], \\ \frac{1}{2}\left[1+\sin\left(\frac{(h+2(\omega-\omega_k))\pi}{2h}\right)\right] & \text{if } \omega \in [\omega_k, \omega_k + h_k], \\ 0 & \text{otherwise,} \end{cases} \quad (5)$$

where ω_k is the center frequency for the k-th filter, h is the bandwidth, and $h_k = \min\{h, \omega_k\}$. These filters have a response that is almost identical to Gabor filters at tuning frequencies higher than 6 Hz. At lower frequencies, the asymetrical response of the spherical quadrature filters preserves their quadrature property, which yields a correct phase estimation. Figure 4 shows the frequency response for Gabor and spherical quadrature filters tuned at 1 Hz and 10 Hz.

The convolution kernel $g_{\omega_k,h}$ of the filters is found as the inverse Fourier transform of $G_{\omega_k,h}$. The filtered signals $F_{j,\omega,e}$ can then be obtained as

$$F_{j,\omega,e}(t) = (g_{\omega,h} \ * \ S_{j,e})(t) = A_{j,\omega,e}(t) \ \exp[i\phi_{j,\omega,e}(t)], \quad (6)$$

from which we can extract the instantaneous phase and amplitude given by

$$A_{j,\omega,e}(t) \quad = \quad \sqrt{\Re^2(F_{j,\omega,e}(t)) \ + \ \Im^2(F_{j,\omega,e}(t))} \quad (7)$$

$$\phi_{j,\omega,e}(t) \quad = \quad \text{atan2}[\Im(F_{j,\omega,e}(t)), \ \Re(F_{j,\omega,e}(t))], \qquad \phi_{j,\omega,e}(t) \in [-\pi, \pi). \quad (8)$$

Estimation of instantaneous phase-lock

Let us consider the following synchrony criterion: two signals with instantaneous phases $\phi_1(t)$ and $\phi_2(t)$ are in synchrony when $\phi_1(t) \approx \phi_2(t)$ for all t in a given time interval. A straightforward measure would be the magnitude of the phase difference $|\phi_1(t) - \phi_2(t)|$. The phase difference can be wrapped between $-\pi$ and π, thus its magnitude is bounded. This makes it easy to obtain a normalized measure based on the phase difference:

$$\mu_{j,\omega,e_1,e_2}(t) = 1 - \frac{1}{\pi}|\text{wrap}(\phi_{j,\omega,e_1}(t) - \phi_{j,\omega,e_2}(t))|, \tag{9}$$

where $\text{wrap}(\phi)$ returns the angle ϕ wrapped to the interval $[-\pi, \pi)$.

Since we are interested in event-related activity, we must determine how significant are the changes of synchrony with respect to the pre-stimulus segment. Following the procedure introduced by Marroquin to estimate the relative changes of EEG amplitudes [Marroquin et al., 2004], we substract the average synchrony in the pre-stimulus segment in order to obtain the relative synchrony X_{j,ω,e_1,e_2}:

$$X_{j,\omega,e_1,e_2}(t) = \mu_{j,\omega,e_1,e_2}(t) - \frac{1}{T_s}\sum_{t'=1}^{T_s} \mu_{j,\omega,e_1,e_2}(t'), \tag{10}$$

where T_s is the length of the pre-stimulus segment. Finally, we take the mean relative synchrony across all trials:

$$Y_{\omega,e_1,e_2}(t) = \frac{1}{N_r}\sum_{j=1}^{N_r} X_{j,\omega,e_1,e_2}(t). \tag{11}$$

Bayesian estimation of significant synchrony

We would like to classify each value of the mean relative synchrony in one of three classes: significantly higher (class $c = 1$), significantly lower (class $c = -1$), or equal ($c = 0$) to the pre-stimulus average. A common technique for classification problems consists of Bayesian estimation with a prior Markov Random Field (MRF) model [Marroquin, 1987]. With this method, one can model the class field $c_{\omega,e_1,e_2,t}$ as a random field with a prior Gibbs distribution of the form

$$P_{MRF}(c) = \frac{1}{Z}\exp\left[-\lambda\sum_C V_C(c)\right], \tag{12}$$

where Z is a normalizing constant and V_C is a potential function that depends only on the values of the sites belonging to the clique C (see [Marroquin, 1987, 2001] for more details). For a classification problem, where c is discrete, a popular model is the Ising model which enforces c to be piece-wise constant. If we consider a first-order neighborhood system, whose cliques are single sites and nearest-neighbor pairs of sites, the Ising potentials are given by:

$$V_{r,s}(c) = \begin{cases} -1, & \text{if } c_r = c_s \\ 1, & \text{if } c_r \neq c_s \end{cases}, \tag{13}$$

where r and s are nearest neighbors. In our case, r and s are generally 4-tuples of the form $r = (\omega, e_1, e_2, t)$; however, at this point we are only interested in modeling persistence in time, although persistence across frequencies and spatial regularization could be taken into account to attempt an automated segmentation process.

The distribution of a field c which is both Markovian (with a first-order Ising model) and has prior probabilities $\alpha_k = P(c_r = k)$ is given by:

$$P_c(c) \quad = \quad \frac{1}{Z} \exp\left[-\lambda \sum_{<r,s>} V_{r,s}(c) + \sum_r \log \alpha_{c_r}\right],$$

where $-\log \alpha_{c_r}$ can be seen as a zero-order potential $V_r(c)$. Besides the prior distribution of c, we also need the likelihood $P(Y \mid c)$ which can be written as

$$P(Y \mid c) = \prod_r P(Y_r \mid c_r) = \exp\left[\sum_r \log P(Y_r \mid c_r)\right]. \tag{14}$$

Using Bayes rule, the posterior distribution of c given Y can be calculated as

$$P(c \mid Y) = \frac{1}{Z'} \exp\left[-\sum_r \log h_r(c_r) + \lambda \sum_{<r,s>} V_{r,s}(c)\right], \tag{15}$$

where Z' is a normalization constant and $h_r(k) = P(Y_r \mid c_r = k)\alpha_k$.

Given the estimator $\hat{c}$ and the true (unknown) field c, one can define a cost function $C(c, \hat{c})$ and find the optimal $\hat{c}$ by minimizing the expected value of $C(c, \hat{c})$. Since c is discrete, a suitable cost function given by Marroquin is

$$C(c, \hat{c}) = \sum_r \left[1 - \delta(c_r - \hat{c_r})\right], \tag{16}$$

and its expected value would be given by

$$\begin{aligned} E\left[C(c, \hat{c})\right] &= \sum_c C(c, \hat{c}) P(c \mid Y) \\ &= \sum_c \sum_r \left[1 - \delta(c_r - \hat{c_r})\right] P(c \mid Y) \\ &= K - \sum_r \sum_{c: c_r = \hat{c_r}} P(c \mid Y). \end{aligned} \tag{17}$$

The posterior marginal distribution for site r is defined as:

$$\pi_r(k) = \sum_{c: c_r = k} P(c \mid Y). \tag{18}$$

Thus the optimal estimator $\hat{c}$ (which minimizes $E[C(c, \hat{c})]$) can be found by maximizing $\pi_r(\hat{c_r})$ for each r. This estimator is known as the Maximizer of Posterior Marginals (MPM) estimator and is usually approximated using stochastic

Markov-chain methods such as Metropolis or the Gibbs sampler. These algorithms, however, are computationally expensive and require an unknown number of iterations, which makes them less than adequate for our multidimensional data set. A better solution consists on approximating the posterior marginal distributions with the *empirical marginals* $p_r(k)$ [Marroquin et al., 2001]. It can be shown that the p_r vectors form a MRF with the same neighborhood system as c, thus the distribution of p is given by

$$P_p(p) = \frac{1}{Z_p} e^{-U(p)}, \tag{19}$$

where, for a first-order neighborhood system, $U(p)$ can be written as

$$U(p) = \sum_r |p_r - \hat{p_r}|^2 + \lambda' \sum_{<r,s>} |p_r - p_s|^2, \tag{20}$$

with $\hat{p_r}(k) = h_r(k) / \sum_{k'} h_r(k')$.

If c follows the Ising model, it can be shown that the field p can be modeled as a set of decoupled membrane models $p(k) = \{p_r(k), \forall r\}$ for $k = -1, 0, 1$. Therefore, the optimal p is obtained by minimizing, for each layer k, the energy function $U_k(p)$ given by

$$U_k(p) = \sum_r (p_r(k) - \hat{p_r(k)})^2 + \lambda' \sum_{<r,s>} (p_r(k) - p_s(k))^2. \tag{21}$$

Since each $p(k)$ is continuous, $U_k(p)$ can be minimized by solving the linear system obtained from equating the partial derivatives of U_k with respect to $p_r(k)$ to zero. However, the optimal $p(k)$ is a smoothed version of $\hat{p}(k)$, thus one can achieve a similar result by simply low-pass filtering each $\hat{p}(k)$ with a Gaussian kernel (for more details see [Marroquin et al., 1997]). Once we have p we can obtain the approximated MPM estimator as

$$c_r = \text{argmax}_k \{p_r(k)\}. \tag{22}$$

Estimation of prior distributions and likelihoods

For now, we are only interested in modeling persistence in time, thus we may estimate the time series $c_{\omega,e_1,e_2}(t) = c_{\omega,e_1,e_2,t}$ in a decoupled manner for each ω, e_1, and e_2. To simplify things in this section, we will consider a fixed frequency ω and electrode pair (e_1, e_2) and only keep the time subindex.

In order to calculate $h_t(k)$ (and thus $p_t(k)$) we need the prior probabilities $\alpha_k = P(c = k)$ and likelihoods $P(Y_t \mid c = k)$. These can be estimated from the data if we consider that the complete distribution $P_Y(Y_t)$ can be expressed as:

$$P_Y(Y_t) = \sum_{k=-1}^{1} \alpha_k P(Y_t \mid c = k), \tag{23}$$

and also consider the following assumptions:

- $P(Y_t \mid c = 0)$ may be estimated empirically from the pre-stimulus data.
- $P(Y_t \mid c = 1) = 0$ for $Y \leq 0$.
- $P(Y_t \mid c = -1) = 0$ for $Y \geq 0$.

With these assumptions, we can obtain $P(c = 0)$ from Equation (23) as follows:

$$\alpha_0 = \frac{P_Y(0)}{P(0 \mid c = 0)} \tag{24}$$

and also

$$h_t(0) = \alpha_0 P(Y_t \mid c = 0) \tag{25}$$

$$h_t(1) = \begin{cases} P_Y(Y_t) - h_t(0), & Y_t > 0 \\ 0, & Y_t \leq 0 \end{cases} \tag{26}$$

$$h_t(-1) = \begin{cases} P_Y(Y_t) - h_t(0), & Y_t < 0 \\ 0, & Y_t \geq 0 \end{cases} \tag{27}$$

$P_Y(Y_t)$ and $P(Y_t \mid c = 0)$ can be estimated from the data Y using non-parametric kernel estimation. $P_Y(Y_t)$ is estimated using the full time segment, whereas $P(Y_t \mid c = 0)$ considers only the pre-stimulus segment.

The actual classification procedure for significative synchrony changes is performed (for each frequency ω and electrode pair (e_1, e_2)) as follows:

1. Estimate the pre-stimulus distribution $P_0(Y)$ and the full distribution $P_Y(Y)$ using kernel density estimation with bandwidth given by Silverman's rule of thumb [Silverman, 1986].
2. Estimate $\alpha_0 = P(c = 0) = P_0(0)/P_Y(0)$.
3. For each t, calculate $h_t(k)$ for $k = -1, 0, 1$ as given by Equations (25, 26, and 27).
4. Normalize h_t to obtain $\hat{p_t}$.
5. Obtain $p(k)$ by convolving $\hat{p}(k)$ with a Gaussian kernel g. The width σ of the kernel controls the granularity of the c field (see below).
6. Approximate the MPM estimator by $c_t = \text{argmax}_k p_t(k)$ for all t.

Granularity and choice of σ

When approximating $p(k)$, we need to use an adequate width σ for the Gaussian kernel to filter out shorter homogeneous segments which may not be significant in terms of persistence, and would instead break a longer segment. One approach consists on defining a granularity function $G(\sigma)$ for a given EEG dataset and see how it behaves with respect to σ. Our choice for G is defined

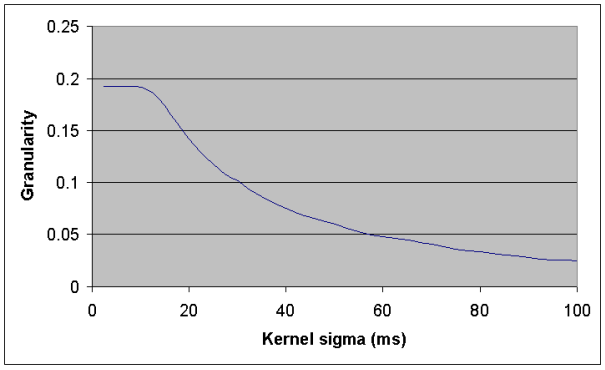

Figure 5: Granularity as defined by Equation (29) for $w = 20$ ms.

as follows: for a class time series $c_{\omega,e_1,e_2} = \{c_{\omega,e_1,e_2}(t)\}$ we define the number of homogeneous segments n_{ω,e_1,e_2} as

$$n_{\omega,e_1,e_2} = \sum_{t=T_s}^{T} I\left[c_{\omega,e_1,e_2}(t) \neq c_{\omega,e_1,e_2}(t-1)\right], \tag{28}$$

where $I(P)$ equals 1 if P is true and zero otherwise. Note that the sum is taken only on the post-stimulus segment. This is because we consider the pre-stimulus to be a single segment with class $c = 0$.

We also define $m_{\omega,e_1,e_2}(w)$ as the number of homogeneous segments whose length is less than w. The granularity is then given by

$$G_w(\sigma) = E\left[\frac{m_{\omega,e_1,e_2}(w)}{n_{\omega,e_1,e_2}}\right], \tag{29}$$

where the expected value is estimated across all frequencies and electrode pairs. $G_w(\sigma)$ estimates the probability of having segments with length shorter than w for a given value of σ. We have chosen to dismiss segments shorter than $w = 20$ ms by aiming for a granularity value of 0.05 or less. Figure 5 shows the graph for $G_{20}(\sigma)$ where a granularity of less than 0.05 is reached with $\sigma = 57.5$ ms for the Figures experiment.

Visualization

We use two types of display to represent the data. The first display shows, for a fixed time t and frequency ω, the classification values $c_{\omega,e_1,e_2,t}$ for all electrode pairs (e_1, e_2). This results in a *multitoposcopic* display ([Jimenez et al., 1995]) of a synchrony pattern as shown in Figure 6.

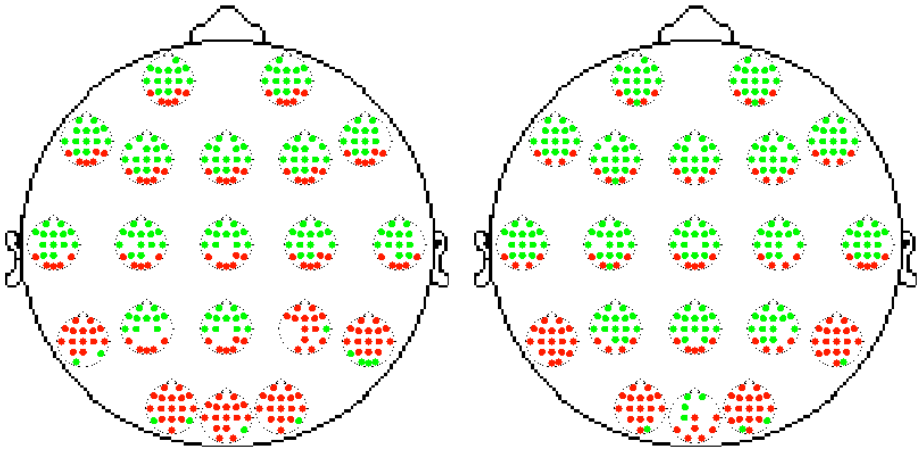

Figure 6: Multitoposcopic representation of synchrony patterns during the Figures experiment at $t = 525$ ms and $f = 11$ Hz estimated with potentials (left image) and virtual cortical sources (right image). These graphs show significant increments (red) or decrements (green) in synchrony with respect to the pre-stimulus segment. Synchronous activity is smeared when using potentials: sites P4 and Oz show a significant increment in synchrony with almost every other site; however, most of these couplings do not show when using VS signals, indicating that they were spurious.

Multitoposcopic displays are useful to show a detailed connectivity pattern for a fixed time and frequency; however, it is important to visualize larger regions of the time-frequency plane in order to localize zones of interest where the synchrony pattern remains almost constant and might be related to specific cognitive processes. Following the procedure given by [Marroquin et al., 2004] to analyze relative amplitude changes, we can use a Time-Frequency-Topography (TFT) display to present the data by reducing only one spatial dimension. We do this not by averaging but counting, for each electrode e, the number of electrodes that have significantly increased or decreased their synchrony with e. In other words, we can build a *synchrony increase histogram* (SIH) given by

$$H^{+}_{\omega,e}(t) \quad = \quad \sum_{e'=1}^{N_e} I(c_{\omega,e,e',t} = 1), \tag{30}$$

where $I(X) = 1$ only if X is true. $H^{+}_{\omega,e}(t)$ is the number of significantly stronger couplings (with respect to the pre-stimulus segment) for electrode e at time t and frequency ω. This can be thought as a degree of connectivity involving electrode e relative to the pre-stimulus.

Similarly, we can define a *synchrony decrease histogram* (SDH) as

$$H^{-}_{\omega,e}(t) \quad = \quad \sum_{e'=1}^{N_e} I(c_{\omega,e,e',t} = -1), \tag{31}$$

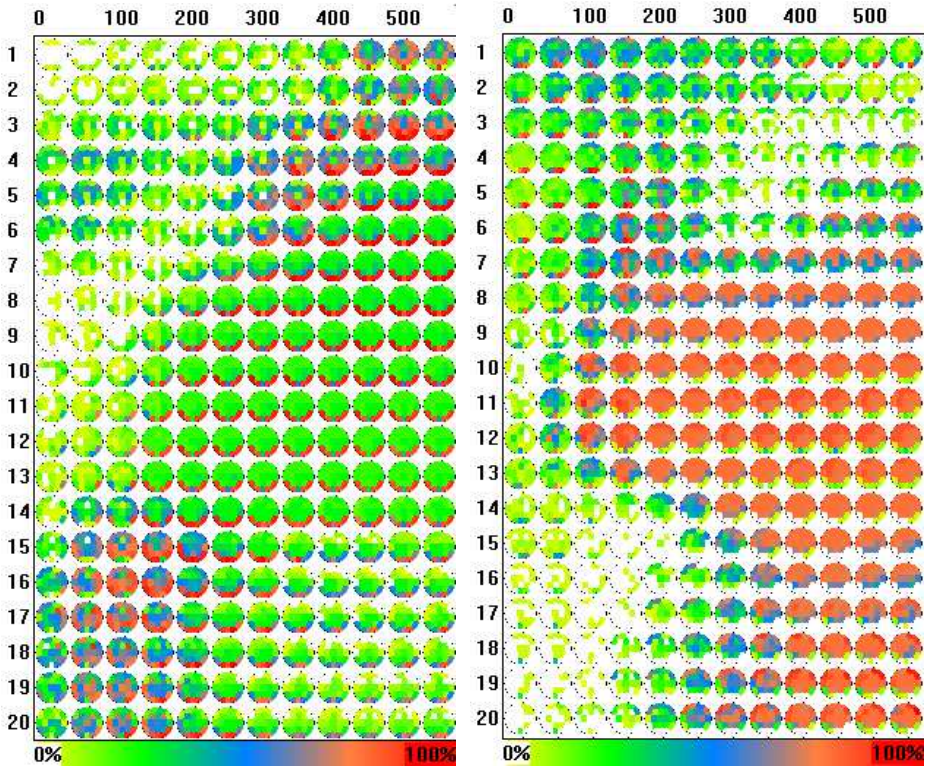

Figure 7: Synchrony histograms for the Figures experiment displayed as Time-Frequency-Topography (TFT) maps. The left and right maps show synchrony increase and decrease histograms, respectively. The scale represents the proportion of electrodes whose synchronization with a given electrode e changes significatively.

These histograms can be presented in a TFT display as shown in Figure 7.

Interactive segmentation

The TFT visualization system provides at the same time a detailed view that shows which regions of the cortex are involved in synchronous processes at any time and frequency, and also a condensed view where one can see larger Time-Frequency regions which share the same synchronization pattern. This allows one to easily perform a manual segmentation of the TF plane where each region is assigned a representative multitoposcopic pattern. An example of a segmented map is shown in Figure 13 for the Figures experiment.

It is also possible to produce an automated segmentation by frequency bands at regular time intervals. An example of this is shown in Figure 8. The frequency bands are delta (1 to 3 Hz), theta (4 to 7 Hz), alpha (8 to 12 Hz) and low beta (13 to 18 Hz) with a segment interval of 300 ms. In the lower-left corner of each

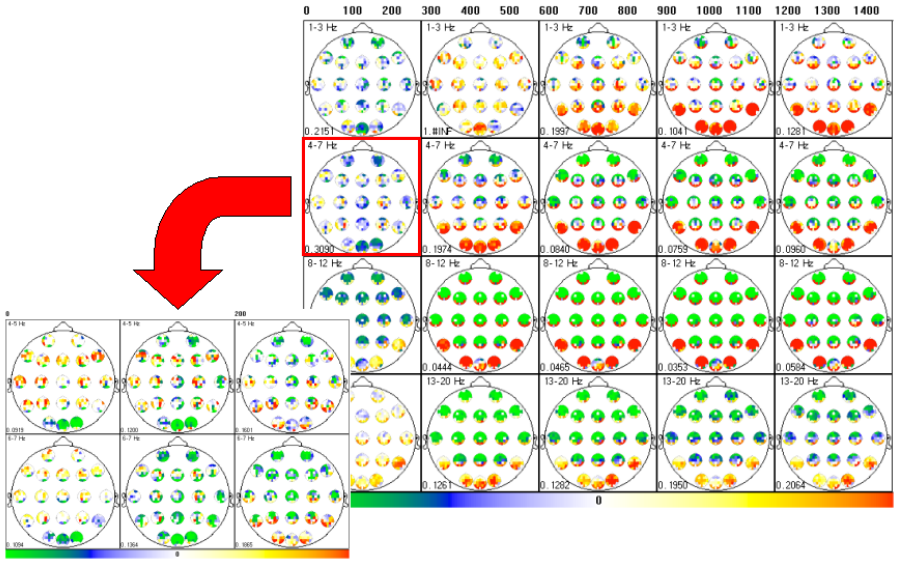

Figure 8: Automatically segmented synchrony maps for the Figures experiment. The color scale represents an average of the relative synchrony between each pair of sites within a time-frequency window: towards red means synchrony increment while towards green means synchrony decrease. Regions with high-variance can be subdivided into smaller, more consistent regions.

segment we show the estimated variance of $c_{\omega,e,e',t}$. Those segments with high variance can be subdivided for a more detailed analysis.

Other synchronization measures

We have tested other syncronization measures in order to make a thorough comparison and determine each measure's strengths and weaknesses. In order to do a comparison following the same methodology, we have substituted the Bayesian class estimation by significance indexes based on the p-values of the mean relative synchrony $Y_{\omega,e_1,e_2}(t)$ with respect to the pre-stimulus distribution.

Synchrony can be defined in a very broad sense as a degree of similarity between two signals. In general, we consider a synchrony measure either a function $\mu_{j,\omega,e_1,e_2}(t)$ that estimates the similarity between F_{j,ω,e_1} and F_{j,ω,e_2} at each time t for trial j, or a function $\mu_{\omega,e_1,e_2}(t)$ that estimates the average similarity between F_{j,ω,e_1} and F_{j,ω,e_2} at each time t across all trials $j = 1, \ldots, N_r$. Whenever possible, we normalized each measure μ between 0 and 1 such that $\mu(t) = 1$ means perfect synchrony.

For each measure we perform a statistical analysis to determine the significance of the changes with respect to the pre-stimulus segment. This analysis involves the following steps:

1. Estimate the average synchrony in the pre-stimulus segment and substract it from the synchrony measure. We call this new variable the *relative synchrony*.
2. Estimate the mean relative synchrony across all trials (if necessary).
3. Estimate the pre-stimulus distribution of the mean relative synchrony.
4. Perform non-parametric statistical tests to estimate the significance level of the mean relative synchrony with respect to the pre-stimulus distribution.

The actual procedure for measures that are estimated for each trial is slightly different for those which use all trials. For those measures of the form μ_{j,ω,e_1,e_2} the relative synchrony X_{j,ω,e_1,e_2} for each trial j is given by

$$X_{j,\omega,e_1,e_2}(t) = \mu_{j,\omega,e_1,e_2}(t) - \frac{1}{T_s}\sum_{t'=1}^{T_s} \mu_{j,\omega,e_1,e_2}(t'), \tag{32}$$

where T_s is the length of the pre-stimulus segment. On the other hand, for measures of the form μ_{ω,e_1,e_2} the relative synchrony is

$$X_{\omega,e_1,e_2}(t) = \mu_{\omega,e_1,e_2}(t) - \frac{1}{T_s}\sum_{t'=1}^{T_s} \mu_{\omega,e_1,e_2}(t'). \tag{33}$$

Next, we average the relative synchrony for those measures that are estimated per trial. This yields the mean relative synchrony Y_{ω,e_1,e_2}:

$$Y_{\omega,e_1,e_2}(t) = \frac{1}{N_r}\sum_{j=1}^{N_r} X_{j,\omega,e_1,e_2}(t). \tag{34}$$

For measures that depend on all trials we simply let $Y_{\omega,e_1,e_2}(t) = X_{\omega,e_1,e_2}(t)$.

Let P_Y be the density function of Y_{ω,e_1,e_2} in the pre-stimulus segment for given ω, e_1, and e_2. By construction we have that $E[Y_{\omega,e_1,e_2}(t)] = 0$ for $t \leq T_s$, hence P_Y is centered at zero. A significative increase in synchrony is given by a positive value of $Y_{\omega,e_1,e_2}(t)$ such that

$$P_Y\left(Y > Y_{\omega,e_1,e_2}(t) \mid Y > 0\right) < \alpha \tag{35}$$

for a given significance threshold $\alpha > 0$. Similarly, a significative decrease in synchrony happens when

$$P_Y\left(Y < Y_{\omega,e_1,e_2}(t) \mid Y < 0\right) < \alpha. \tag{36}$$

Based on this, we estimate the significance level $S_{\omega,e_1,e_2}(t)$ of the mean relative synchrony as follows:

$$S_{\omega,e_1,e_2}(t) = \begin{cases} 1 - P_Y(Y > Y_{\omega,e_1,e_2}(t) \mid Y > 0) & \text{for } Y_{\omega,e_1,e_2}(t) > 0, \\ -\left(1 - P_Y(Y < Y_{\omega,e_1,e_2}(t) \mid Y < 0)\right) & \text{for } Y_{\omega,e_1,e_2}(t) < 0. \end{cases} \tag{37}$$

S_{ω,e_1,e_2} ranges from -1 to 1. Positive values indicate an increase in synchrony with respect to the pre-stimulus segment, while negative values indicate a decrease in synchrony. Values with a magnitude greater than $(1-\alpha)$ are said to be significant. Common values for α are 0.05 and 0.01.

We will now define the measures we have tested.

Phase locking statistic (PLS)

This measure estimates the instantaneous variability of the phase difference of two signals across trials. Since we are working with a phase distribution, we must use the concept of circular variance [Fisher, 1995] which can be estimated as

$$\mathrm{Var}(\phi) \approx 1 - \frac{1}{N}\left|\sum_{n=1}^{N} \exp[i\phi_n]\right|, \tag{38}$$

where $\phi_1, \ldots, \phi_N$ is a sample from the distribution of ϕ. The circular variance is always between 0 and 1 so $1 - \mathrm{Var}(\phi)$ can be used as a measure of phase coherence. Lachaux et al. proposed as synchrony measure the circular variance of phase differences across trials at instant t and called it *phase locking statistic* (PLS) [Lachaux et al., 1999]:

$$\mu_{\omega,e_1,e_2}(t) = \left|\frac{1}{N_r}\sum_{j=1}^{N_r} \exp[i(\phi_{j,\omega,e_1}(t) - \phi_{j,\omega,e_2}(t))]\right|, \tag{39}$$

where N_r is the number of trials in the EEG experiment.

Single-trial phase locking statistic (STPLS)

In order to obtain a phase locking measure to single trials, Lachaux et al. proposed a new measure based on the variance of the phase difference across a time window centered at time t, for each trial j [Lachaux et al., 2000]:

$$\mu_{j,\omega,e_1,e_2}(t) = \left|\frac{1}{2w+1}\sum_{t'=t-w}^{t+w} \exp[i(\phi_{j,\omega,e_1}(t') - \phi_{j,\omega,e_2}(t'))]\right|, \tag{40}$$

This measure follows this particular synchrony criterion: two signals with instantaneous phases $\phi_1(t)$ and $\phi_2(t)$ when $\phi_1(t) - \phi_2(t)$ is approximately constant for all t in a given time window. We have used a window size of 100 ms ($w = 10$ samples) in all our tests.

Coherence

Statistical coherence is a measure of how closely two time series are related by a linear transformation [Gardner, 1992] and it is widely used as a measure of EEG synchrony [Bressler et al., 1993, 1995; Nunez, 1995; Gross et al., 2001]. For

two zero-mean signals X and Y, coherence C_{XY} is obtained as the magnitude of their correlation:

$$C_{XY} = \frac{|R_{XY}|}{|R_{XX}R_{YY}|^{1/2}} \tag{41}$$

with

$$R_{XY} = E\{XY^*\} \tag{42}$$

where $E\{\cdot\}$ denotes expected value and Y^* is the complex conjugate of Y. Coherence takes values between 0 and 1 where $C_{XY} = 1$ means Y can be obtained as a linear transform of X.

In order to estimate a coherence measure for a set of filtered EEG signals $F_{j,\omega,e}$ we must first substract their mean across the whole time segment:

$$F'_{j,\omega,e}(t) = F_{j,\omega,e}(t) - \sum_{t'=1}^{N_t} F_{j,\omega,e}(t'). \tag{43}$$

Then for each trial j we take the coherence on a time window around time t, thus the coherence measure can be defined as

$$\mu_{j,\omega,e_1,e_2}(t) = \frac{|R_{j,\omega,e_1,e_2}(t)|}{|R_{j,\omega,e_1,e_1}(t)R_{j,\omega,e_2,e_2}(t)|^{1/2}} \tag{44}$$

where

$$R_{j,\omega,e_1,e_2}(t) = \frac{1}{2w+1} \sum_{t'=t-w}^{t+w} F'_{j,\omega,e_1}(t')(F'_{j,\omega,e_2}(t'))^*, \tag{45}$$

for each time t and electrode pair (e_1, e_2). A window size of 100 ms was also used for coherence measures.

Cumulative probability of phase difference (CPPD)

An alternative to the measure defined by Equation (9) consists on estimating the probability of the phase difference being smaller (in absolute value) than some $\epsilon > 0$. This probability can be estimated across trials and equals the proportion of trials where the magnitude of the phase difference $\phi_{j,\omega,e_1}(t) - \phi_{j,\omega,e_2}(t)$ is less than ϵ for each t, ω, e_1, and e_2:

$$\mu_{\omega,e_1,e_2} = \frac{1}{N_r} \sum_{j=1}^{N_r} I(|\text{wrap}(\phi_{j,\omega,e_1}(t) - \phi_{j,\omega,e_2}(t))| < \epsilon). \tag{46}$$

where $I(P)$ equals 1 if P is true, and zero otherwise.

This measure allows a quantification of the degree of synchrony (by means of ϵ), regardless of any further transformation applied to the measure (such as the significance analysis we perform).

Mutual information and Generalized Synchronization

Two other measures that are often mentioned in EEG synchrony literature (i.e.- Quian-Quiroga et al., 2002; David et al., 2004) are Generalized Syncronization (GS) and Mutual Information (MI).

GS relies upon vectors $\vec{X}_n = [x_n, x_{n+\tau}, \ldots, x_{n+(m-1)\tau}]$ which are embeddings of the signal x in an m-dimensional space with a delay time τ. If p_{ni} and q_{ni}, $i = 1, \ldots, k$, denote the indices of the k nearest neighbors of $\vec{X}_n$ and $\vec{Y}_n$, respectively, then one can define a measure of closeness $S_n^k(X|Y)$ between the true neighbors $\{\vec{X}_{p_{ni}}\}$ of $\vec{X}_n$ and its mutual neighbors $\{\vec{X}_{q_{ni}}\}$ (for more details see [Quian-Quiroga, 2002]). The synchronization statistic is the average of $S_n^k(X|Y)$ over a time window $t - T \leq n \leq t + T$.

On the other hand, Mutual Information is a statistical measure which estimates, for two random variables X and Y, the amount of information in X given that Y is known, and viceversa. It is defined as $MI(X,Y) = H(X) + H(Y) - H(X,Y)$, where $H(X)$ is the statistical entropy of X and $H(X,Y)$ is the joint entropy of X and Y (see [David et al., 2004] for details). MI basically measures the similarity between the histograms of X and Y (estimated, in our case, across a time window) and it does not take into account any possible time lag between both signals. This makes it unadequate as a phase-locking measure. It is possible, however, to apply time-embedding techniques (taking as sample data the vectors $\vec{X}_n$ used in GS) to obtain a lag-sensitive MI measure [Quian-Quiroga et al., 2002].

There are two aspects that make these measures inadequate for our procedure: first, as a result of the time-embedding methods, these measures have low time resolution (hundreds of milliseconds) and are better suited for the analysis of stationary couplings. Second, they are computationally very demanding, which makes them hard to integrate in an interactive TFT exploration system. For these reasons we do not include them in the following comparison.

Comparison between synchrony measures

Figures 9 and 10 show the syncrony increase histograms for the CPPD, PLS, STPLS, and coherence measures. It is clear that CPPD and PLS give very similar results to the mean phase difference measure (Figure 7, left). On the other hand, STPLS and coherence yield similar results themselves but different from MPD. The estimated correlation between each pair of measures (Figure 11, left) confirms what we see. It is worth noting that similar correlation results were also obtained with five different experiments besides the Figures experiment presented here (see Appendix A).

Seemingly, we have two groups of synchrony measures, thus it is important to understand what kind of similarities between signals are being quantified by each group, and how measures from the same group are related to each other. One thing to note is that STPLS and coherence are defined across a time window, while the other measures are instantaneous. Another issue is that in the STPLS measure (Equation 40), if one of the phases remains fairly constant across the time window, then this measure will be related to the circular variance of the

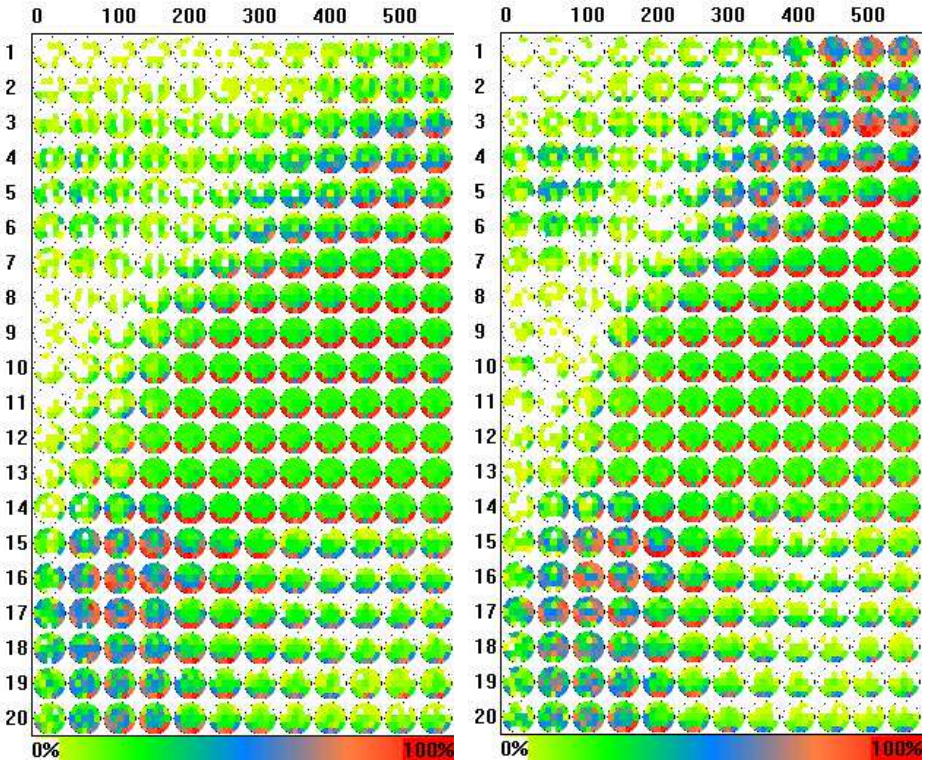

Figure 9: Synchrony increase histograms for the Figures experiment using the CPPD (left) and PLS (right).

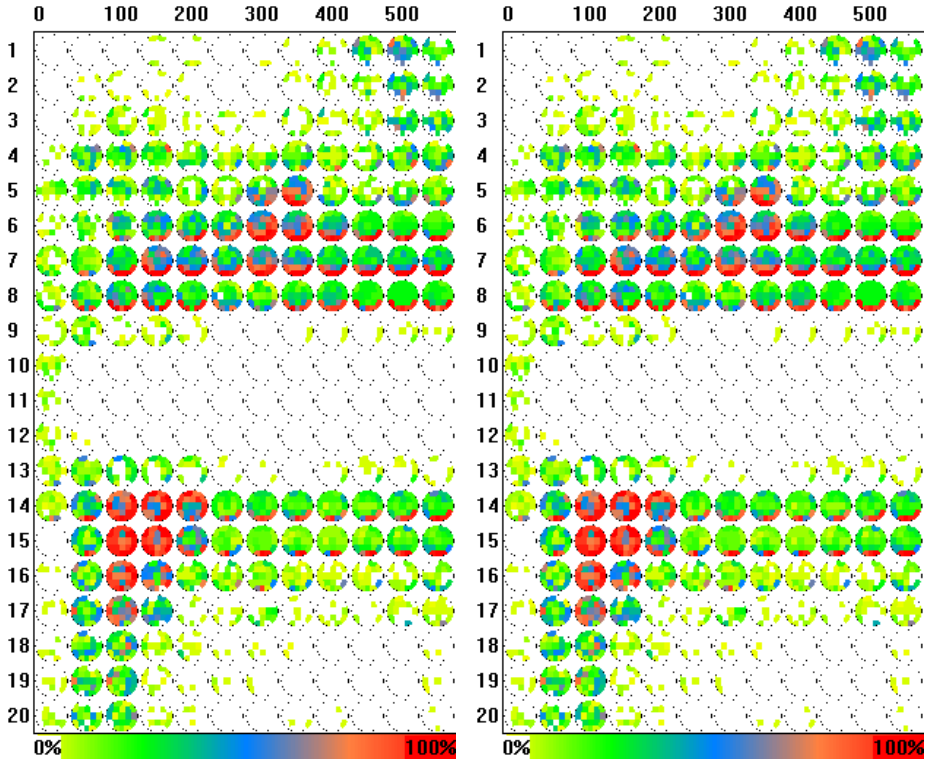

Figure 10: Synchrony increase histograms for the Figures experiment using the STPLS (left) and coherence (right).

	MPD	CPPD	PLS	STPLS	Coherence
MPD	1	0.916	0.987	0.403	0.535
CPPD	0.916	1	0.899	0.378	0.501
PLS	0.987	0.899	1	0.409	0.541
STPLS	0.403	0.378	0.409	1	0.932
Coherence	0.535	0.501	0.541	0.932	1

	LPD
MPD	0.138
CPPD	0.113
PLS	0.174
STPLS	0.8
Coherence	0.719

Figure 11: Correlation between pairs of synchronization measures (left), and between synchronization measures and local phase dispersion (right). There are clearly two groups of measures: those similar to the MPD, and those similar to the STPLS. The latter group is characterized by a high correlation with LPD.

other phase. To see how much this variance influences the STPLS we estimated a local phase dispersion (LPD) measure given by

$$LPD_{j,\omega,e}(t) = \frac{1}{2w+1}\left|\sum_{t'=t-w}^{t+w} \exp\left[i\phi_{j,\omega,e}(t')\right]\right|. \tag{47}$$

Then we estimated a correlation between the LPD and the average synchrony in each electrode for all the measures (Figure 11, right). Effectively, both STPLS and coherence show a high correlation with LPD. This leads one to think that these measures are not well-suited for detecting long-range synchronization, but may in fact quantify some form of "local" synchrony . To explain this with further detail we introduce a simple model.

EEG population model

This model is based on the assumption that the signal captured by each electrode is the sum of the contributions of a population of neurons in the cortical region corresponding to the virtual source. We see each neuron as a simple sinusoidal oscillator whose frequency is fixed but whose phase can change over time. For simplicity, we assume all neurons oscillate with amplitude 1. The VS corresponding to each electrode e covers a population of N_e neurons, thus the signal f_e registered by the electrode and projected to the cortex can then be obtained by

$$f_e(t) = \sum_{j=1}^{N_e} \cos(\omega_{ej}t + \phi_{ej}(t)), \tag{48}$$

where ω_{ej} and $\phi_e j$ are the frequency and phase, respectively, of each oscillator in the population. If we band-pass filter f_e around center frequency ω and with sufficiently narrow bandwidth, we can approximate the filtered signal $f_{\omega e}$ by

$$f_{\omega e}(t) = \sum_{j=1}^{N_{\omega e}} \cos(\omega t + \phi_{ej}(t)), \tag{49}$$

where $N_{\omega e}$ is the number of neurons oscillating at frequency ω in the population.

Suppose these neurons are divided in sub-populations that are in perfect synchrony; that is, all neurons in each sub-population oscillate with the same phase. The phases form a finite set $\{\phi^1, \ldots, \phi^K\}$, with K being the number of sub-populations. We allow neurons to change their phase but they must synchronize themselves with another sub-population. This translates into the following model:

$$f_{\omega e}(t) = N_{\omega e}\sum_{k=1}^{K} \alpha_{\omega e}^k(t)\cos(\omega t + \phi^k), \qquad \sum_{k=1}^{K}\alpha_{\omega e}^k = 1, \qquad \alpha_{\omega e}^k \geq 0, \tag{50}$$

where $\alpha_{\omega e}^k(t)$ represents the proportion of neurons in sub-population k.

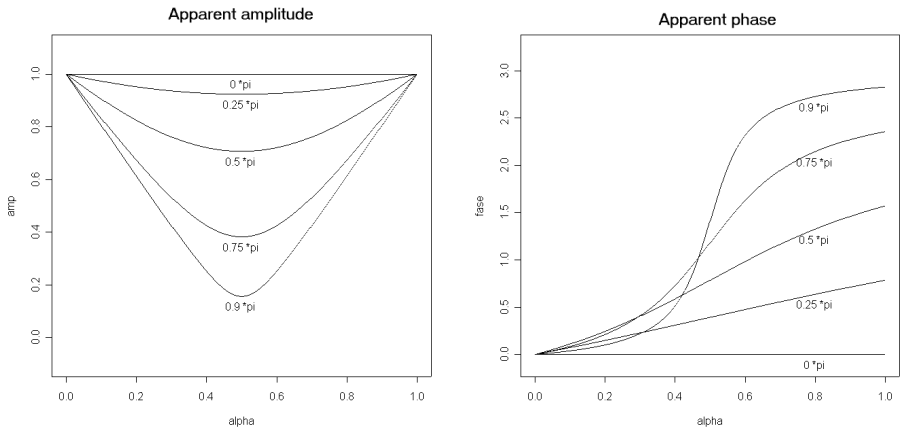

Figure 12: Apparent amplitude and phase versus underlying phase difference $\phi^1 - \phi^2$ and proportion α of oscillators with phase ϕ^1 for a 2-population model.

We define the *apparent* amplitude $A^*_{\omega e}$ and phase $\phi^*_{\omega e}$ of $f_{\omega e}(t)$ as those that would be obtained from passing f through a bandpass quadrature filter tuned at ω. In the case of Gabor filters, they are given by

$$A^*_{\omega e} \exp[i\phi^*_{\omega e}] = N_{\omega e} \sum_{k=1}^{n} \alpha^k_{\omega e} \exp[i\phi^k]. \tag{51}$$

In other words, the apparent amplitude and phase are those of the resultant of the sum of vectors $\alpha^k_{\omega e} \exp[i\phi^k]$. Particularly, for $K = 2$ we have that

$$(A^*_{\omega e})^2 = N^2_{\omega e}(a^2 + b^2), \tag{52}$$

$$\tan \phi^* = b/a, \tag{53}$$

with

$$a = \alpha_{\omega e} \cos \phi^1 + (1 - \alpha_{\omega e}) \cos \phi^2, \tag{54}$$

$$b = \alpha_{\omega e} \sin \phi^1 + (1 - \alpha_{\omega e}) \sin \phi^2. \tag{55}$$

Figure 12 shows (for $K = 2$) how the apparent amplitude and phase vary with respect to the phase difference $(\phi^1 - \phi^2)$ and proportion $\alpha_{\omega e}$. Note that according to this model, a decrease of amplitude may be caused by a local resynchronization process where a group of neurons change their phase resulting in a more uniform proportion of sub-populations.

According to this, variations in the apparent phase may be related either to variations in the phase of some sub-populations (lack of local synchronization), or to changes in the size proportions (which may be considered as local resynchronization processes). With this in mind, we could consider the local phase dispersion (as defined by Equation 47) as a measure of local synchrony.

Consistency of the proposed measure

By looking at Equation (39) one can see that PLS actually measures the consistence of the phase difference across all trials. We have also shown that the MPD and PLS measures are highly correlated. This suggests that the processes that result in high synchronization (as measured by MPD) are fairly consistent across trials and subjects, and thus may be related to the task.

Furhtermore, the CPPD measure is also highly correlated to the MPD, suggesting that synchronization effectively happens with near-zero phase difference. This is in accordance with the neural mass model proposed by David and Friston, where a bidirectional coupling of two remote cortical areas present a phase-locking of zero or π radians [David and Friston, 2003]. Other works (Friston et al., 1997; Rodriguez et al., 1999) have also found zero-centered phase difference distributions during synchronous episodes between two electrodes. These findings lead us to believe the MPD is a suitable long-range synchronization measure.

Example case

A full analysis of the Figures experiment is presented here as an example of the methodology. The full segmented MPD map is presented in Figure 13 along with the corresponding SIH and SDH maps (Figures 14 and 15, respectively). TFT maps of significant changes in amplitude and LPD are also shown in Figures 16 and 17, respectively.

There are a few interesting correlations between MPD, amplitude, and LPD taking place at different frequency bands. In the delta band (1 to 3 Hz) we first see a pattern (50 to 400 ms) characterized by a desynchronization of frontal and parietal sites and a synchronization mostly between O1 and O2. This is accompained by an increase of amplitude in the frontal region and a decrease in the temporal-occipital region. From 400 to 800 ms the syncrony with occipital electrodes increases, particularly with Oz which acts as a nodal point (that is, one that shows synchrony with a large cortical area); at the same time a power increase takes place in an extended frontal-parietal region around 500 ms. After 800 ms the amplitude remains high only at Fp2 but the power decrease in the occipital region remains. The MPD pattern shows a stable high synchrony of every site with the temporal-occipital region.

In the theta band (4 to 7 Hz) we have an early pattern (0 to 150 ms) that shows fronto-parietal synchrony with a significant power increase in every site. From 300 to 600 ms there is a global synchrony increase with the temporal-occipital sites and a power decrease in the same region. After 800 ms the amplitude decreases in the parietal-occipital region with sporadic bursts in Fp2, F3, Fz, Cz, and T4. Global synchrony with the temporal-occipital region is also present, along with desynchronization between frontal and parietal areas. There is an increase in the LPD measure (which means a decrease of local phase variance) around 7 Hz, especially in occipital sites.

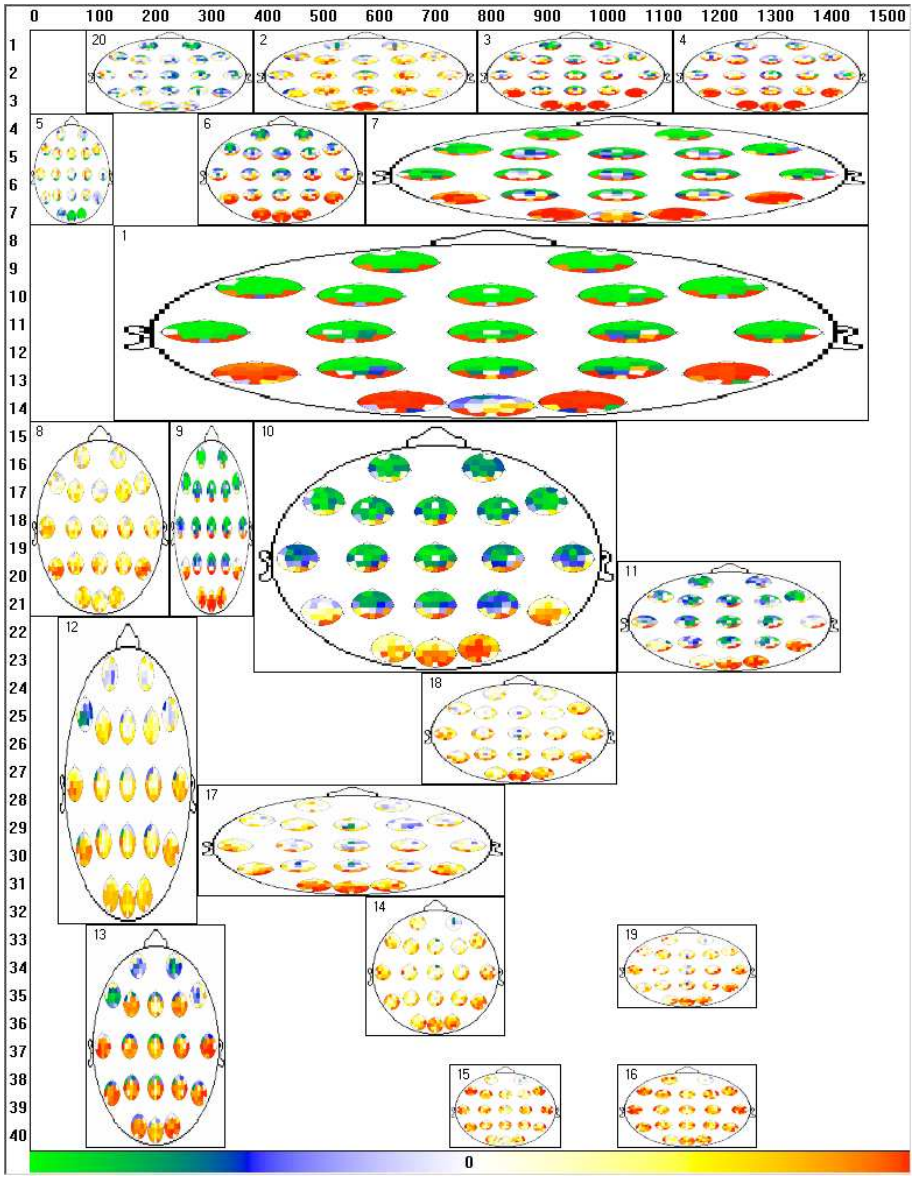

Figure 13: Full manual segmentation for the Figures experiment. The color scale indicates average synchrony increase (towards red) or decrease (towards green) for each pair of sites across each time-frequency window.

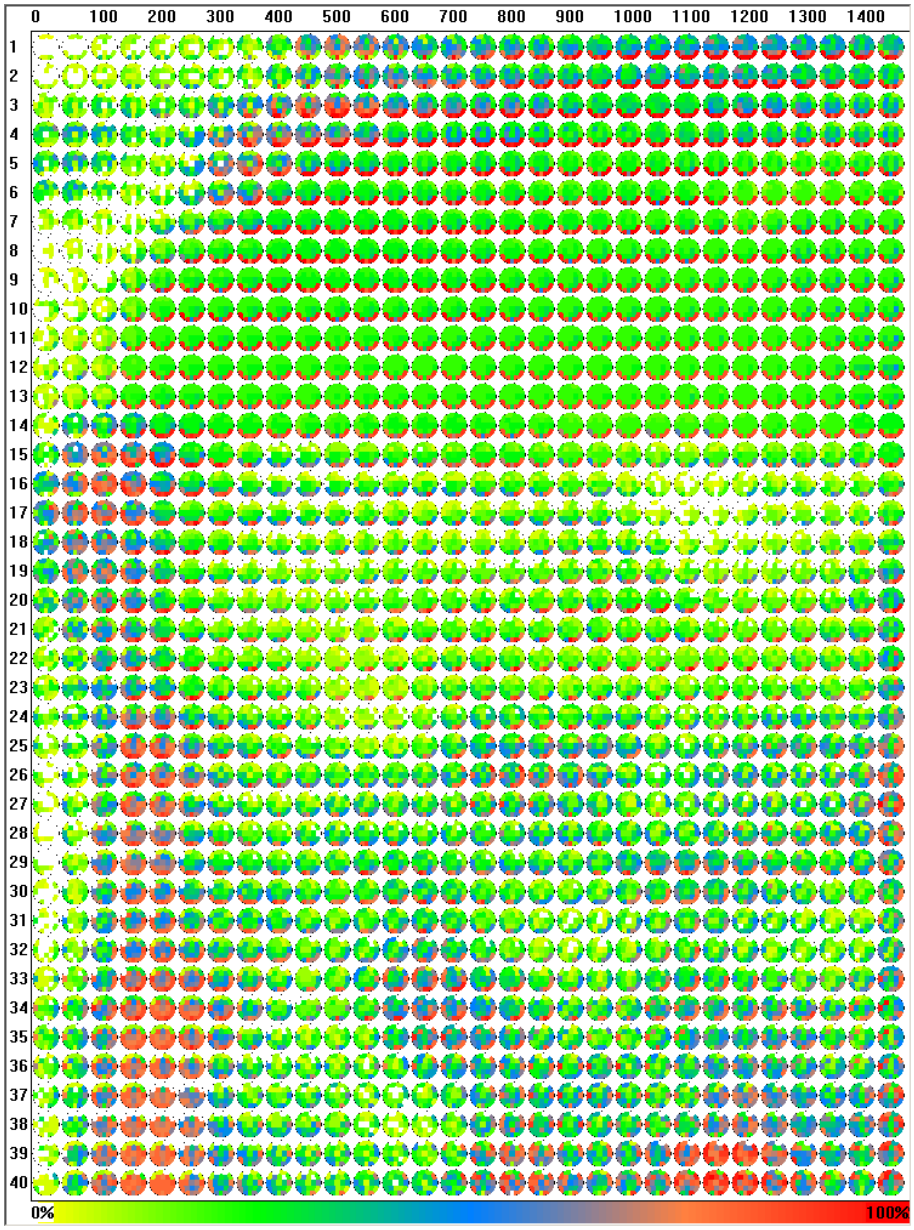

Figure 14: Full synchrony increase histogram for the Figures experiment.

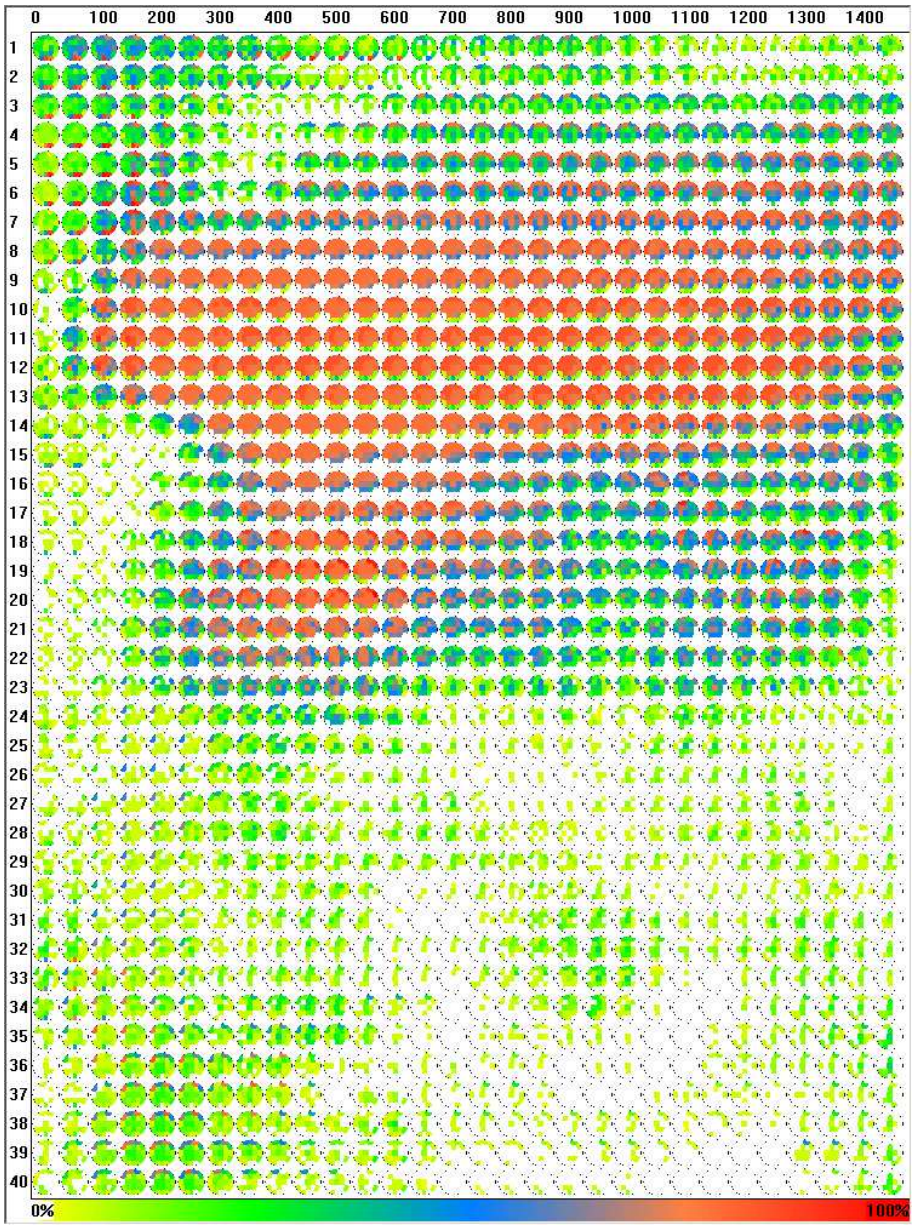

Figure 15: Full synchrony decrease histogram for the Figures experiment.

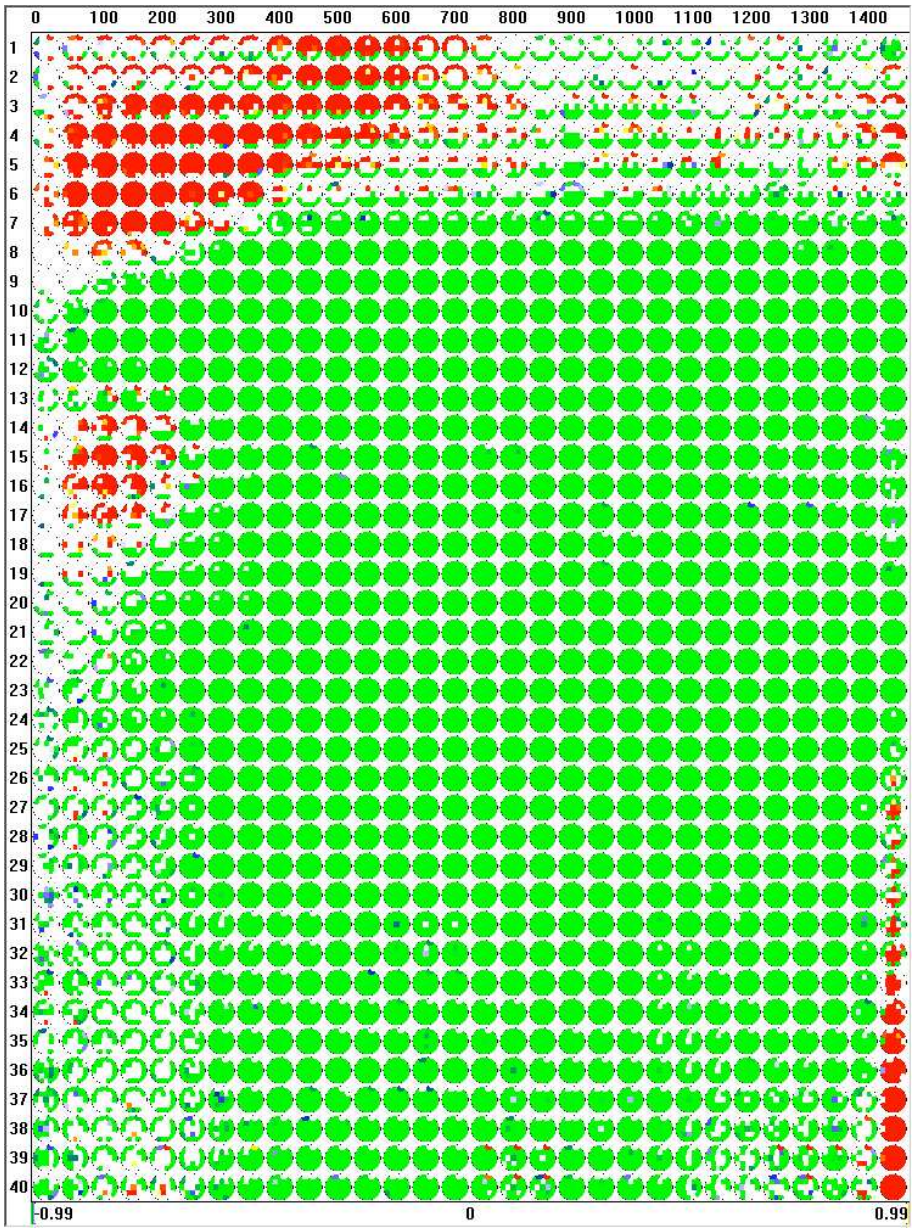

Figure 16: Map of significant amplitude changes for the Figures experiment: sites whose amplitude is significantly higher than the pre-stimulus average are shown in red while those with significantly lower amplitud are shown in green.

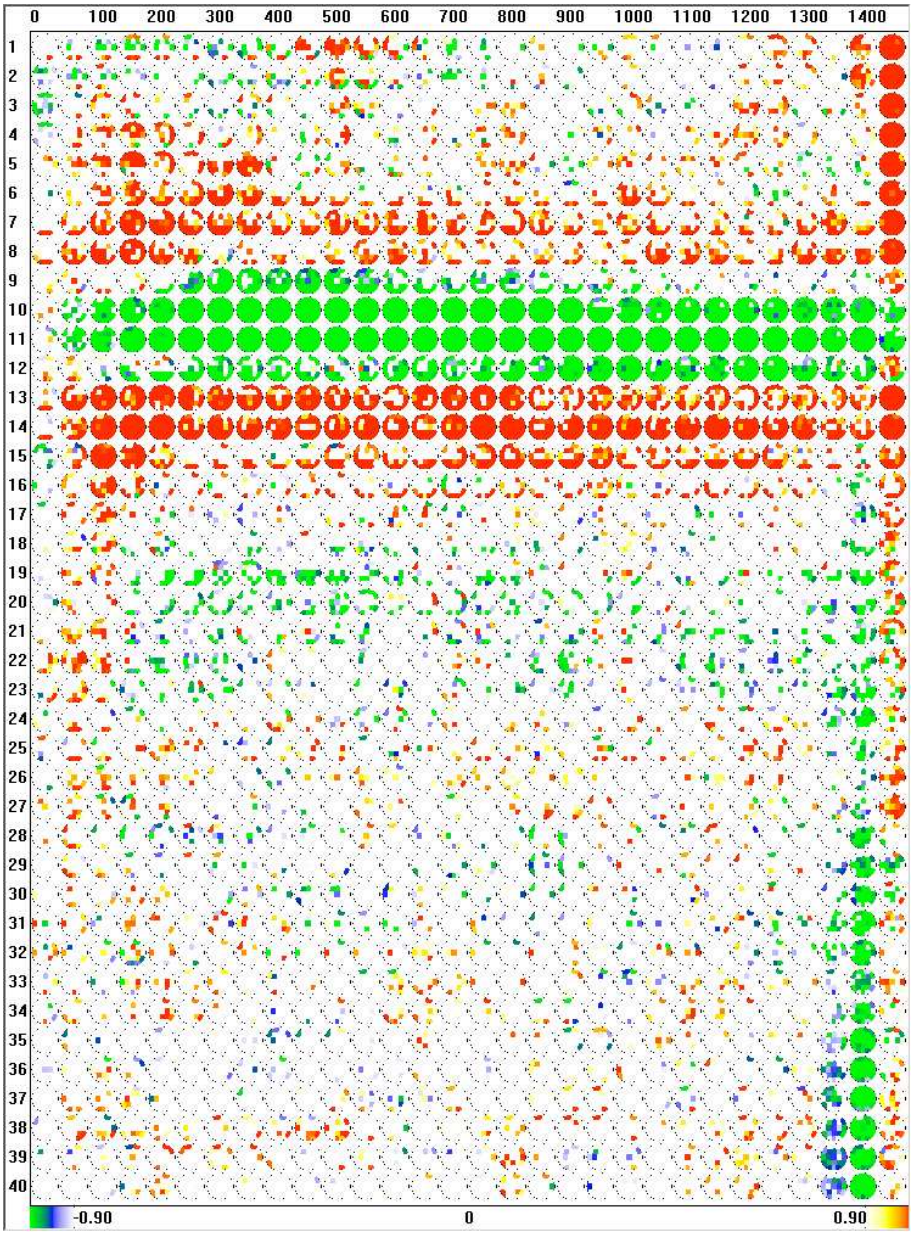

Figure 17: Map of significant LPD changes for the Figures experiment. Red regions have significantly higher LPD measure (that is, less phase dispersion) than the pre-stimulus average, and viceversa for green regions.

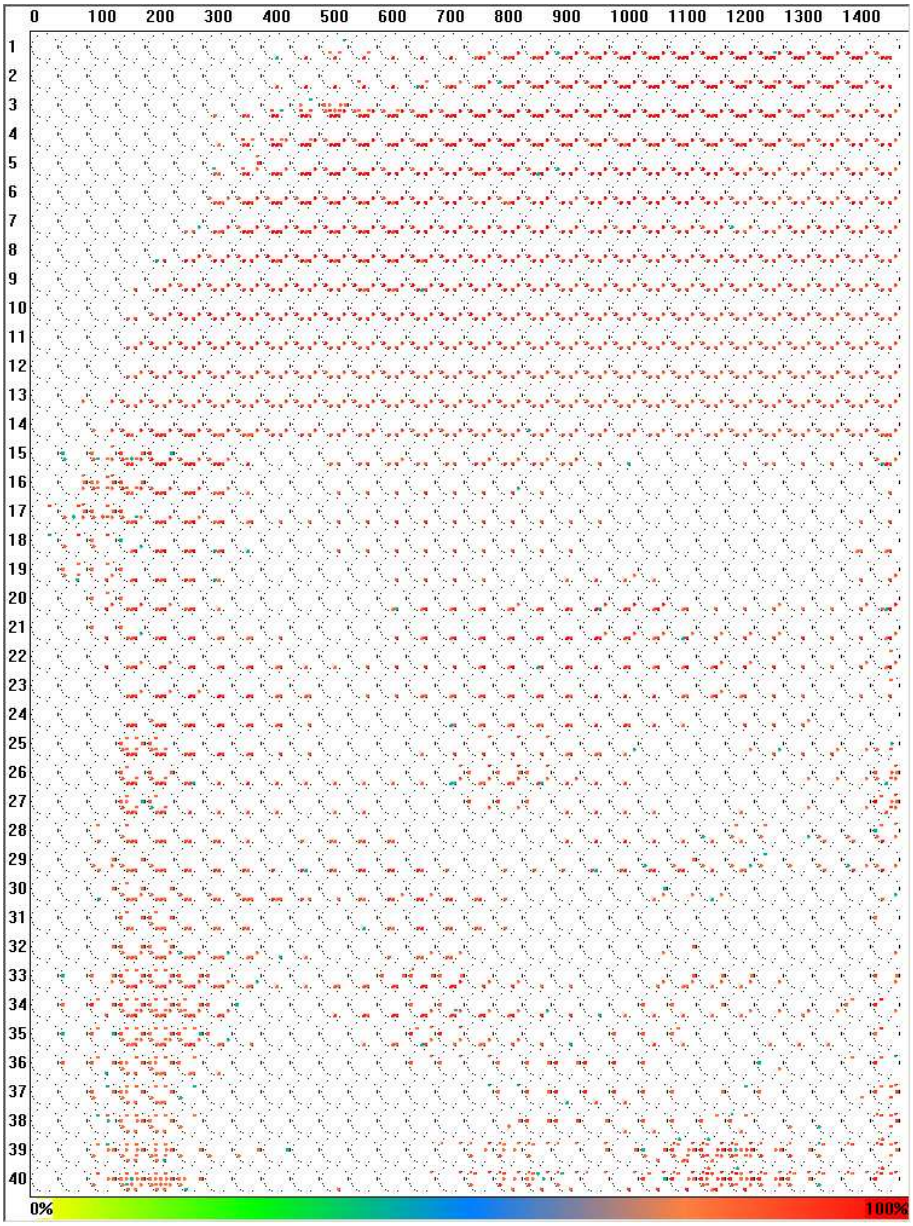

Figure 18: TFT display of 15-nodal sites for the Figures experiment. Each site which is not white is synchronized with at least 15 other sites.

The alpha band shows a very consistent pattern from 200 ms until the end of the experiment. There is a global decrease in amplitude and increased synchrony with the temporal-occipital region. Frontal, central, and temporal areas show a decrease in synchrony between themselves. We have found this characteristic alpha-band pattern in other various experiments. Additionally, a highly consistent (both in time and topography) increase of phase variance takes place at 10 and 11 Hz.

Another early pattern takes place in the low beta band (15 to 20 Hz, 0 to 250 ms) showing frontal, parietal, and temporal increase in amplitude with occipital power decrease, and a global increase of synchronization. After 250ms, this behavior changes to a pattern very similar to that of the alpha band, although not as consistent in terms of synchrony. The upper beta band (20 to 30 Hz) shows high synchrony from 100 to 250 ms with short burst of amplitude in various electrodes at different frequencies. After 250 ms there is a global amplitude drop and a characteristic synchrony increase with occipital sites (especially Oz and O2) with extended synchronous activity in different TF windows (regions 17 and 18 in Figure 13). Phase variance decreases globally at 13 and 14 Hz, and mainly in the occipital sites at 15 Hz.

Early activity in the gamma band (30 to 40 Hz) is very similar to the upper beta band, with an increase of synchronous activity from 50 to 300 ms. Later we find different synchronization patterns involving temporal-occipital areas (regions 14 and 19), temporal-parietal-occipital (region 15), and all sites except Fp2 (region 16).

There are a few interesting observations: first, the image gestalt formation ocurring around 200 ms may be correlated with a significant increment in large-scale, long-range synchrony, mainly in the beta and gamma range. This activity is accompained by a significant power increase in the low beta band. Second, the identification (naming) process might be characterized by a power increase in theta (300 to 600 ms) and synchronous activity which involves occipital nodal points. Third, the preparation of the motor response is probably related to increased synchronous activity in the lower gamma range (around 34 Hz, 600 to 800 ms). Finally, the overall process from 200 ms until the end of the experiment is characterized by synchronous activity with occipital nodes which also display a power decrease in the theta, alpha, and beta ranges, and also later (from 800 ms) in the delta band.

We have also observed that for nodal points connected to sites that show little or no synchronization among them, the relative increase in synchrony is usually correlated with a significant power decrease. To study this in detail, we define a site e as k-nodal at time t and frequency ω if it shows significant increase in synchronization with at least k different sites. Figure 18 shows all 15-nodal sites for the Figures experiment. Let N_k be the number of k-nodal points in the TFT space and A_k^- the number of k-nodal points that also show a power decrease, then the conditional probability of significant power decrease given that a site is k-nodal can be estimated by $P_k^- = A_k^-/N_k$. One may similarly estimate the probability of amplitude increment P_k^+. These probabilities are shown in Figure 19, where it is clear that P_k^- increases with the number of

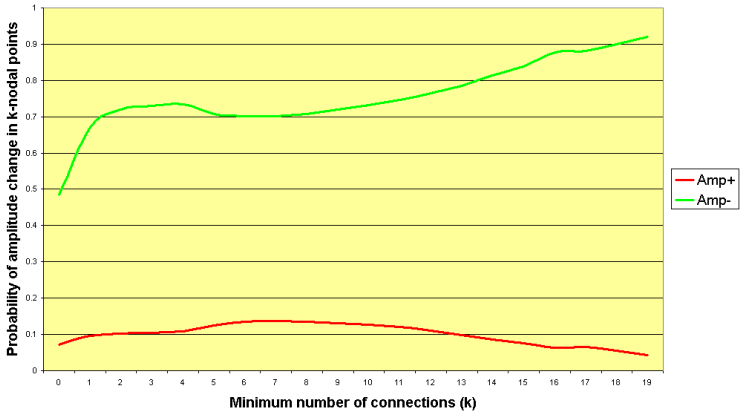

Figure 19: Conditional probabilities of amplitude increment (red) and decrease (green) in k-nodal points.

couplings k.

This behaviour may be explained with the EEG population model: suppose the population covered by the nodal point is divided into various sub-populations, each one of which is coupled with a different site (see Figure 20). If the sites to which the nodal point is connected are not in synchrony, the underlying sub-population phases may assumed to be fairly different. In other words, the underlying phases $\{\phi^j\}$ will show high dispersion, which will be reflected as a low apparent amplitude $A^*_{\omega e}$ (Equation 51). Figure 21 shows a synthetic example which simulates a nodal point placed at O2. The particular model for each virtual source VS_e is given by

$$VS_e(t) = \sum_{k=1}^{N_k} \alpha_{e,k} \cos(\omega t + \phi_k) + \epsilon_e(t), \qquad \epsilon_e(t) \sim \mathcal{N}(0, \sigma_\epsilon) \tag{56}$$

with $N_k = N_e$, $\omega = 10$ Hz (for this example), $\sigma_\epsilon = 0.02$, and underlying phases $\phi_k \sim \mathcal{U}(-\pi, \pi), k = 1, \ldots, N_k$. In the pre-stimulus segment, neurons under site e oscillate predominantly with phase ϕ_e, thus there is little synchronous activity. This may be accomplished by assigning $\alpha_{e,e}$ a higher value than $\alpha_{e,k}, k \neq e$ for each $e = 1, \ldots, N_e$. Specifically, we have that

$$\alpha_{e,k} = \begin{cases} |\eta_{e,k}|, \eta_{e,k} \sim \mathcal{N}(0, \sigma) & \text{if } k \neq e, \\ 1 - \sum_{k \neq e} \alpha_{e,k} & \text{if } k = e. \end{cases} \tag{57}$$

with $\sigma = 0.01$ for this particular example.

In the post-estimulus we model site e_{nod} as a nodal point by increasing the proportion of sub-populations with phases $\phi_k, k \neq e_{\text{nod}}$ (at the expense of a

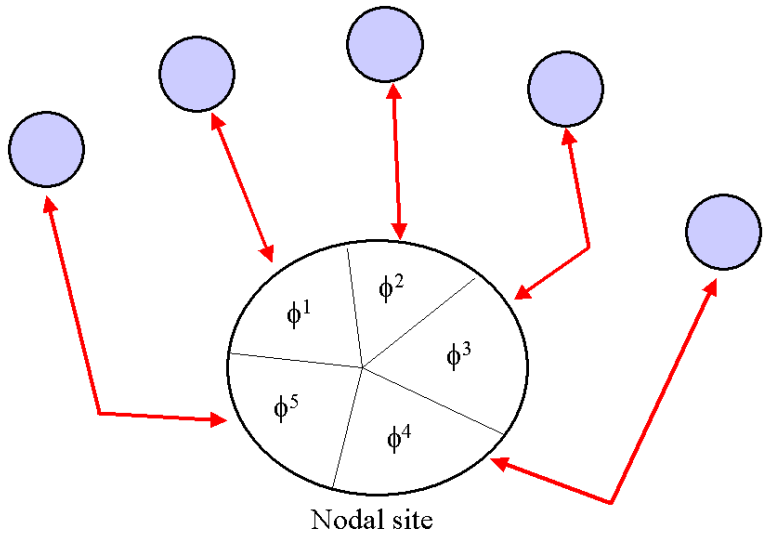

Figure 20: Population model applied to a nodal point: each sub-population under the nodal site is coupled with a different site (shown in blue). The blue sites show no interaction between themselves thus the phases $\{\phi^j\}$ may be different enough to originate a drop in the nodal point's apparent amplitude.

lower $\alpha_{e_{\text{nod}},e_{\text{nod}}}$). This will also cause a drop in the nodal site's amplitude, just as expected. The $\alpha_{e_{\text{nod}},k}$'s in our example are almost uniformly distributed:

$$\alpha_{e_{\text{nod}},k} = \begin{cases} |\frac{1}{N_e} + \eta'_{e_{\text{nod}},k}|, \eta'_{e_{\text{nod}},k} \sim \mathcal{N}(0,\sigma) & \text{if } k \neq e_{\text{nod}}, \\ 1 - \sum_{k\neq 1} \alpha_{e_{\text{nod}},k} & \text{if } k = e_{\text{nod}}. \end{cases} \tag{58}$$

Additionally, we have modeled a syncrony decrease among all non-nodal sites by halving the variance of the α_{ek}'s in Equation (57) (only for non-nodal sites in the post-estimulus segment). This can be seen as a resynchronization process where half the neurons of each sub-population k under site e change their phase from ϕ_k to ϕ_e, which results in a decrease in synchrony with site k.

Conclusion

Brain electroencephalographic activity changes as a function of state. During the performance of different tasks, several neuronal assemblies become active simultaneously. These neuronal networks are not necessarily contiguous and may occupy different cortical areas producing complex spatiotemporal patterns of synchronization or desynchronization in relation to a previous state. Zero phase measurements between leads indicate that the EEG recorded in such leads became highly synchronized and may be integrating a network related to a particular psychophysiological process. Thus, phase relationships between

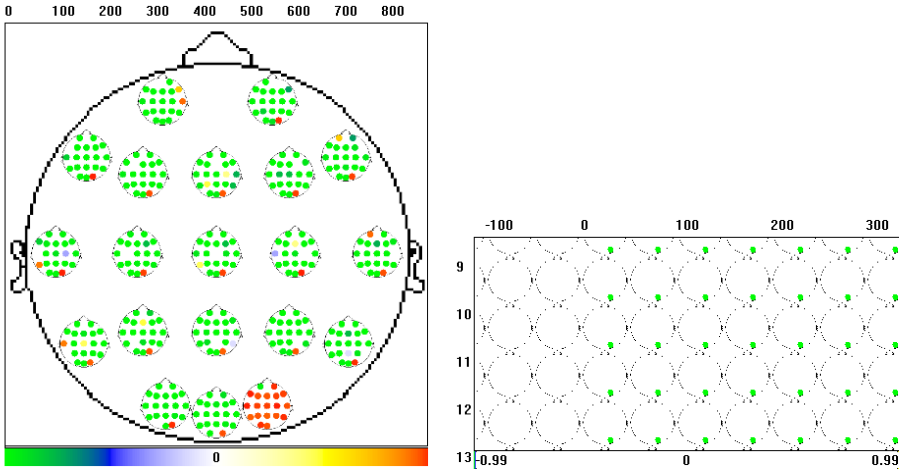

Figure 21: Synthetic example of a nodal point generated (O2) with the population model. The left graph represents the average synchrony pattern obtained in the alpha band for the post-stimulus segment. The right graph shows the amplitude map from -100 to 300 ms (0 ms being the time of stimulus onset) where there is a clear amplitude drop in the nodal site.

regions may give important information about the dynamics of different cell assemblies.

The detection of these phase relationships must be performed with care: some of the common methods such as CSD estimation and coherence may introduce artifacts in the phase and/or synchrony measurements, and thus may not be the most adequate for detecting long-range synchrony. Our procedure effectively avoids these problems by combining a cortical projection technique, spherical quadrature filters, and Bayesian classification of an instantaneous phase-lock measure. On the other hand, TFT visualization techniques have proven to be very useful for the analysis of cognitive tasks as they allow for a quick and interactive exploration of the TF plane while still providing spatial detail. The new insights in the Figures experiment and the nodal sites are examples of the usefulness of these tools.

Appendix A

We have tested our method with five other experiments besides the Figures experiment. Here we present the following maps (post-stimulus segments only) for each experiment: automatically segmented synchrony map, SIH, SDH, amplitude map, and LPD map (Figures 22 through 46). Detailed analysis for some of these experiments will be presented in forthcoming papers.

Words experiment. This is similar to the Figures experiment (Harmony et al., 2001) with the exception that words instead of figures are presented on the screen. The subjects are instructed to press one button if the word corresponds

to an animal and starts with a consonant, and another button if the word does not correspond to an animal and starts with a consonant. If the words starts with a vowel, the subject must not respond.

3-digit and 5-digit Sternberg experiments [Harmony et al., 2004]. A visual warning stimulus (lasting 300 ms) is presented at the start of each trial. After two seconds, a set of three or five digits (memory set) is presented for 1500 ms. Two seconds later, a single digit (probe stimulus) is displayed for 300 ms. The subject must respond with one button if the probe was in the memory set, and with another button if it was not. In 50% of the trials, the number belonged to the memory set. The EEG was sampled each 5 ms with reference to linked ears from Fp1, Fp2, F3, F4, C3, C4, P3, P4, O1, O2, F7, F8, T3, T4, T5, T6, Fz, Cz, Pz, and Oz. Segments of 1280 ms were selected immediately before the memory set was presented (pre-segment) and immediately before the presentation of the probe stimulus (post-segment). Only correct responses and artifact-free segments were analyzed.

Letters experiment. This task is designed to study the inhibition of the motor response. A series of uppercase letters are shown, one at a time, on the screen. The interval between the presentation of one letter and the next one is two seconds. The subject is instructed to respond with a button only if a 'X' that has been preceded by an 'O' appears. This is the Go condition. Any letter different than 'X' which has been preceded by an 'O' accounts for the NoGo condition, as it may originate the inhibition of the motor response. EEG was recorded each 5 ms from Fp1, Fp2, F3, F4, C3, C4, P3, P4, O1, O2, F7, F8, T3, T4, T5, T6, Fz, Cz, and Pz. Each segment was selected from 1 s immediately before the presentation of each letter (pre-segment) to 1560 ms immediately after (post-segment).

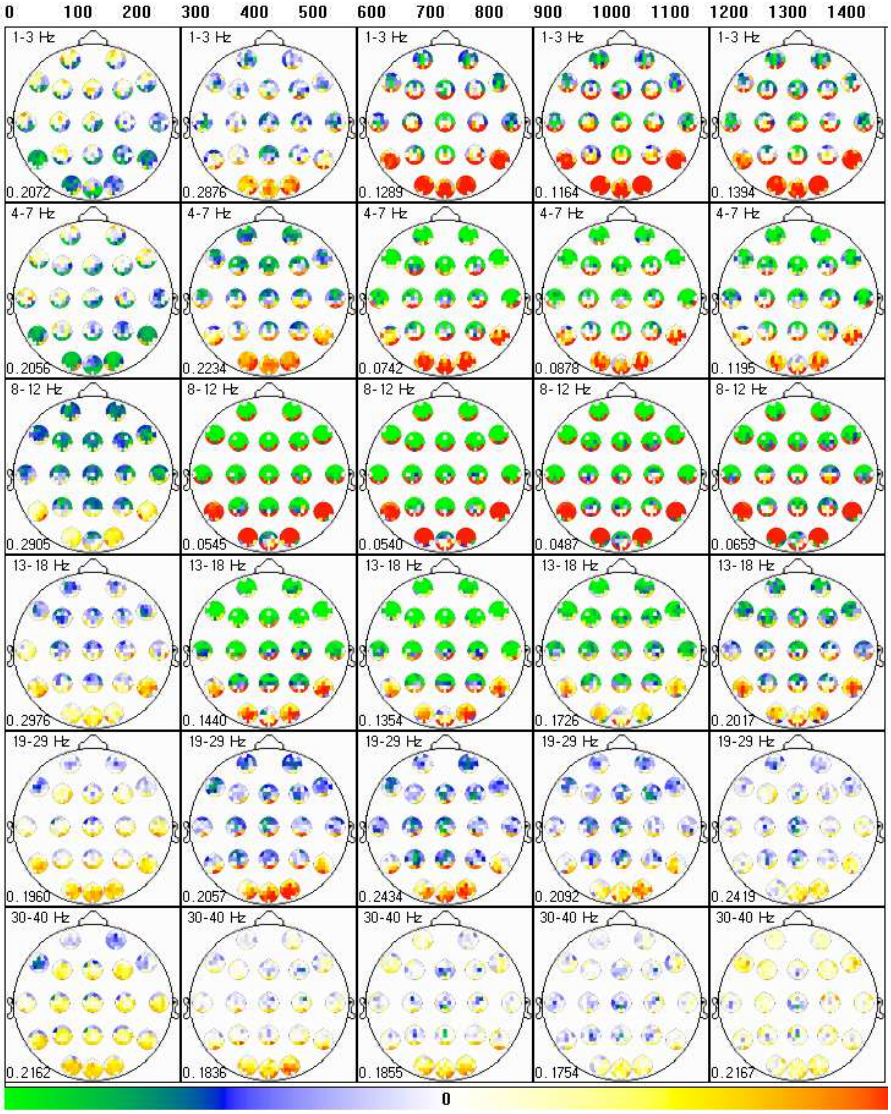

Figure 22: Full automatic segmentation for the Words experiment.

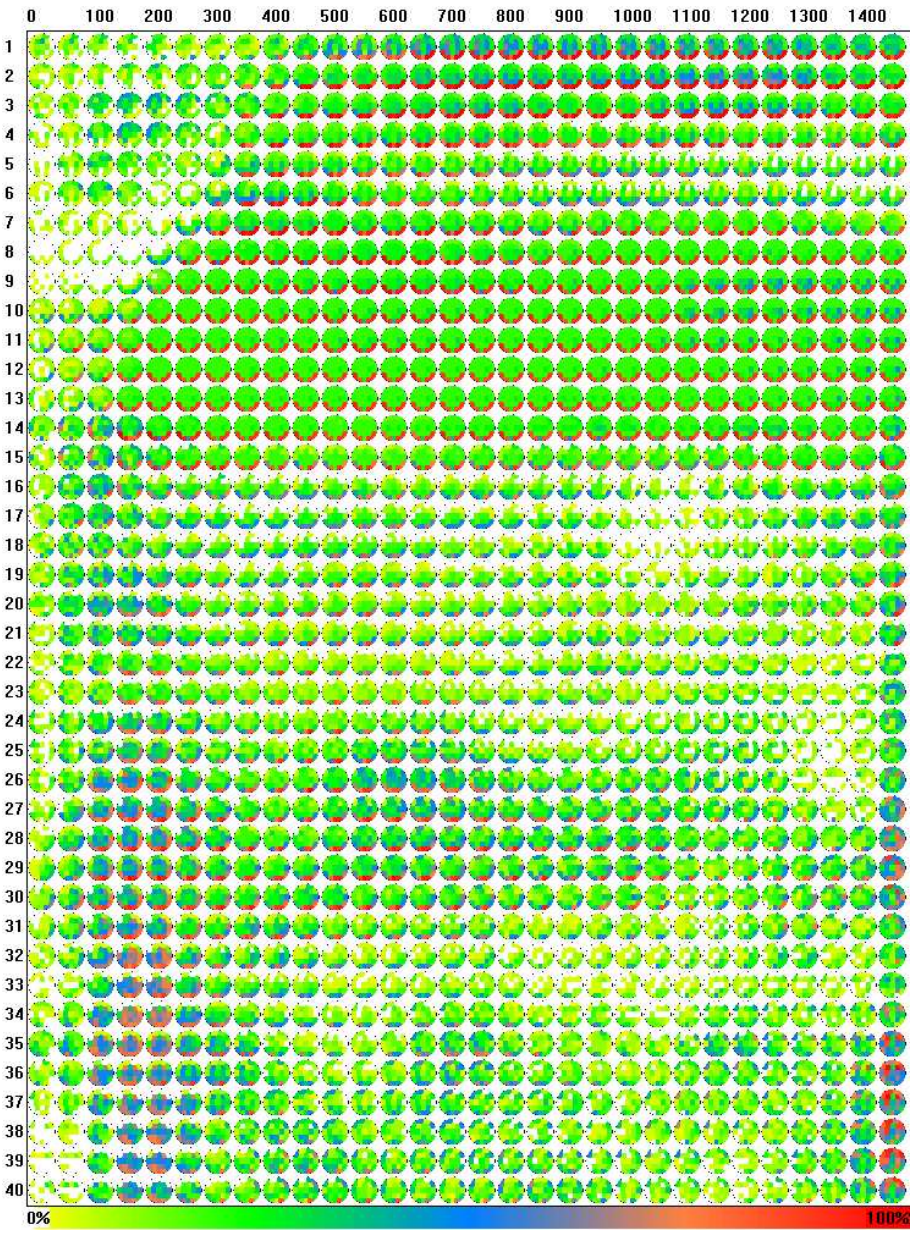

Figure 23: Full synchrony increase histogram for the Words experiment.

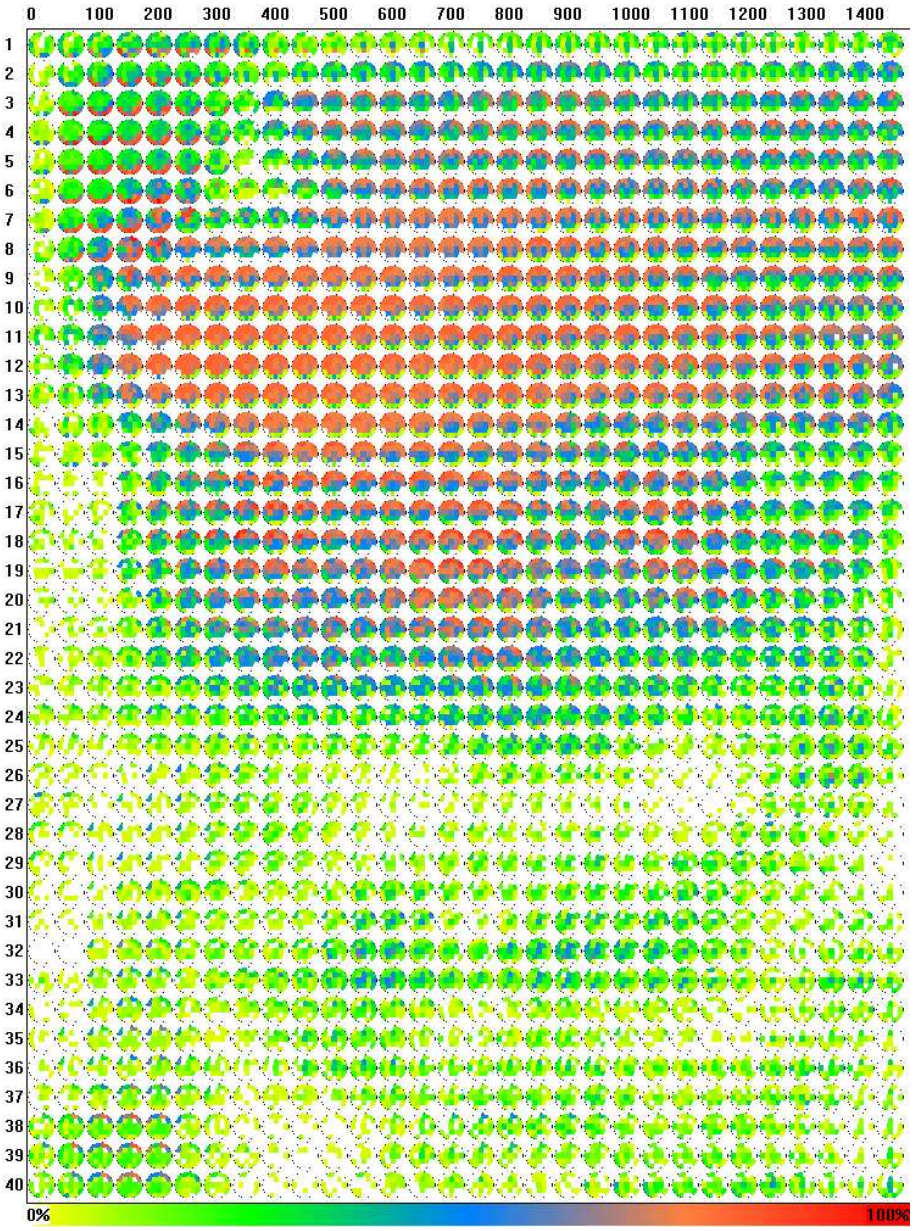

Figure 24: Full synchrony decrease histogram for the Words experiment.

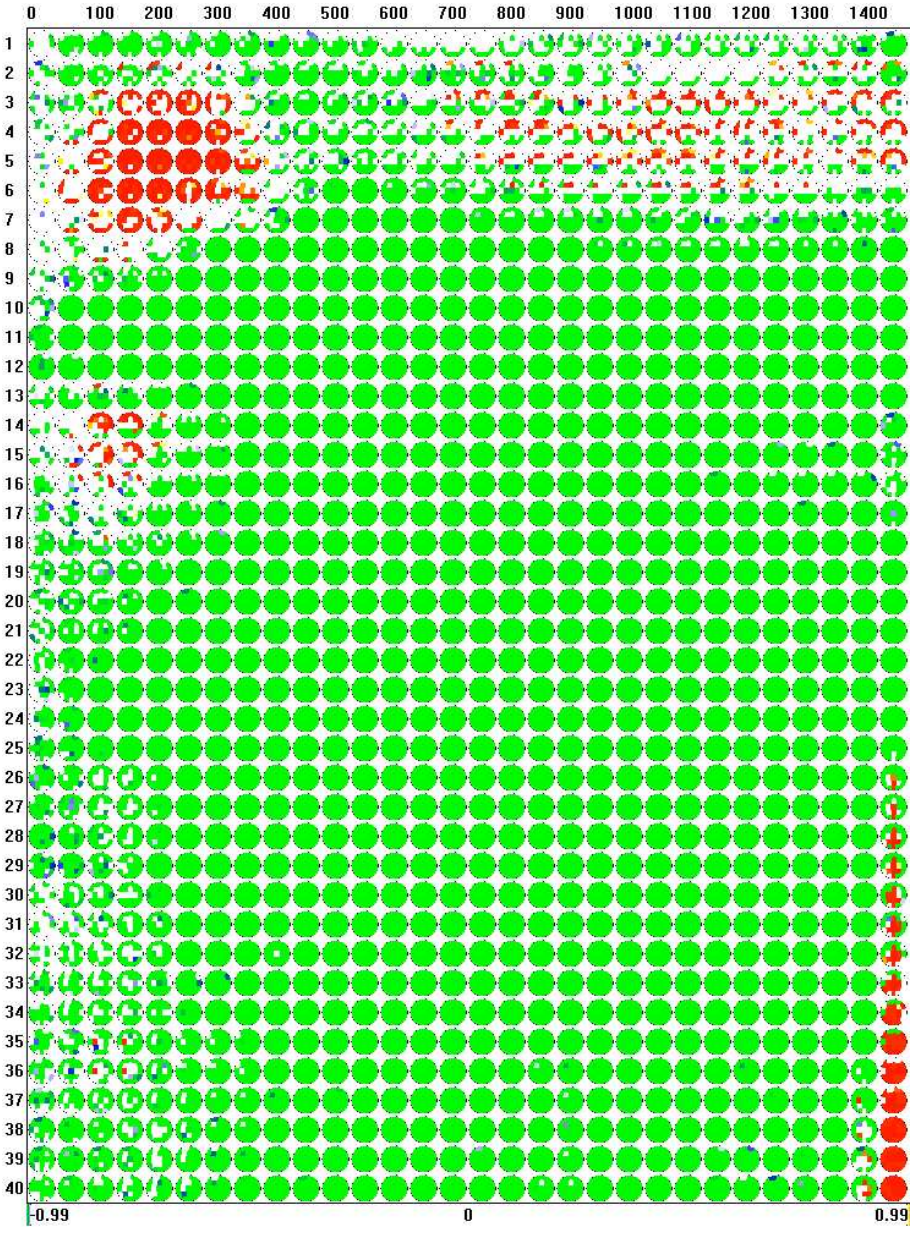

Figure 25: Map of significant amplitude changes for the Words experiment.

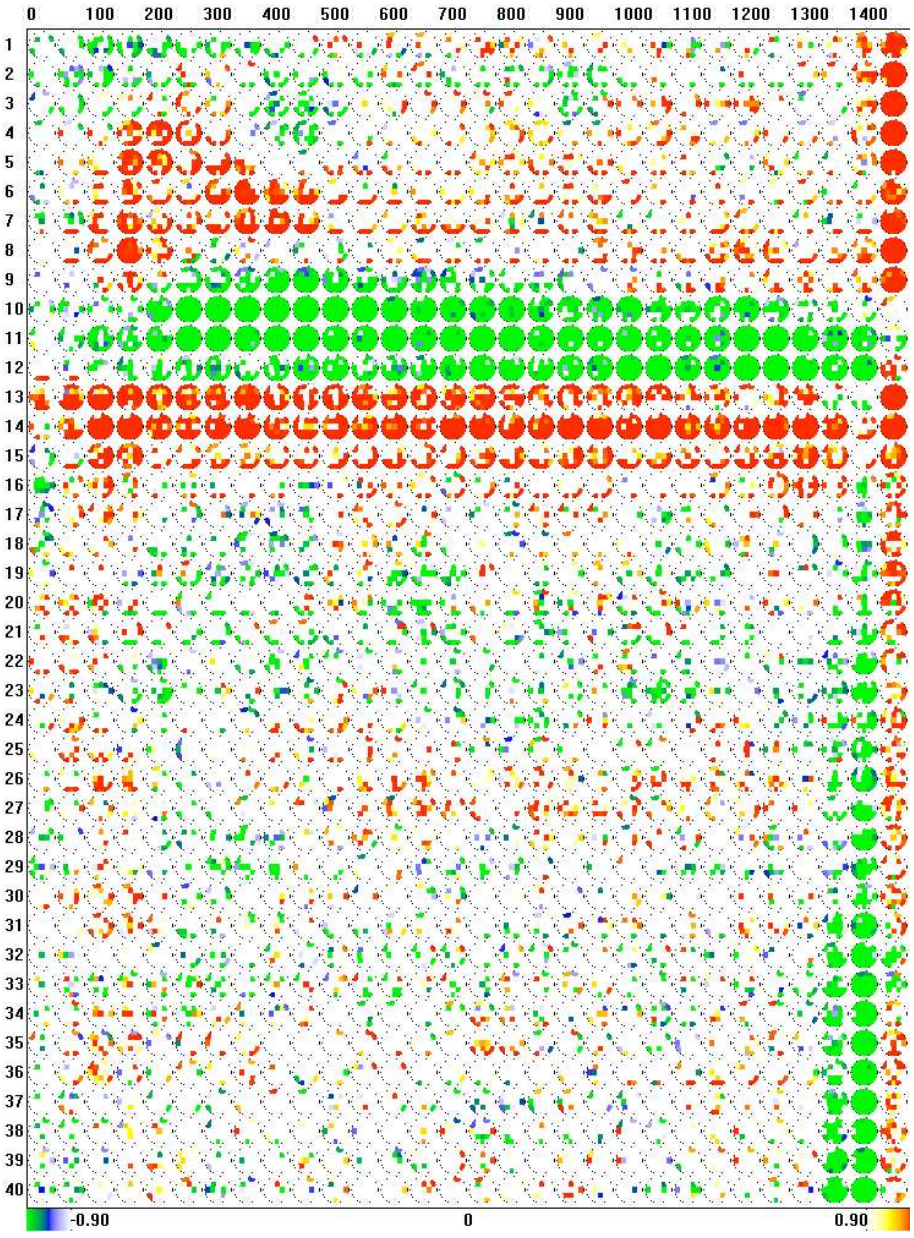

Figure 26: Map of significant LPD changes for the Words experiment.

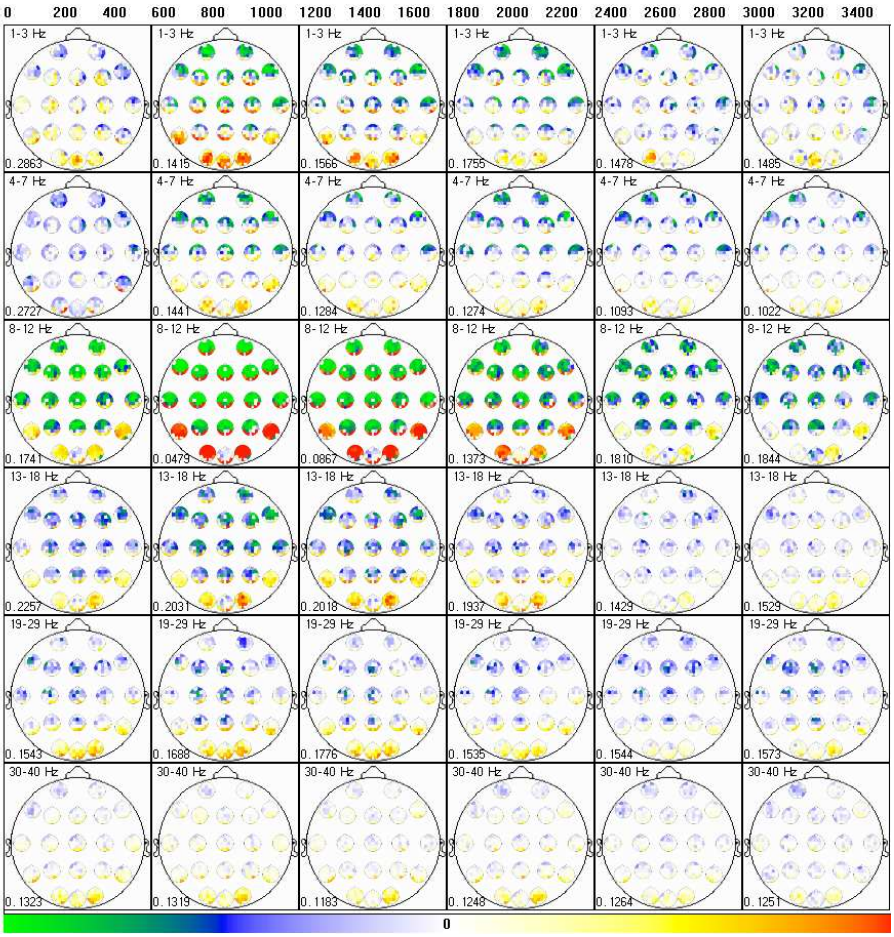

Figure 27: Full automatic segmentation for the 3-digit Sternberg experiment.

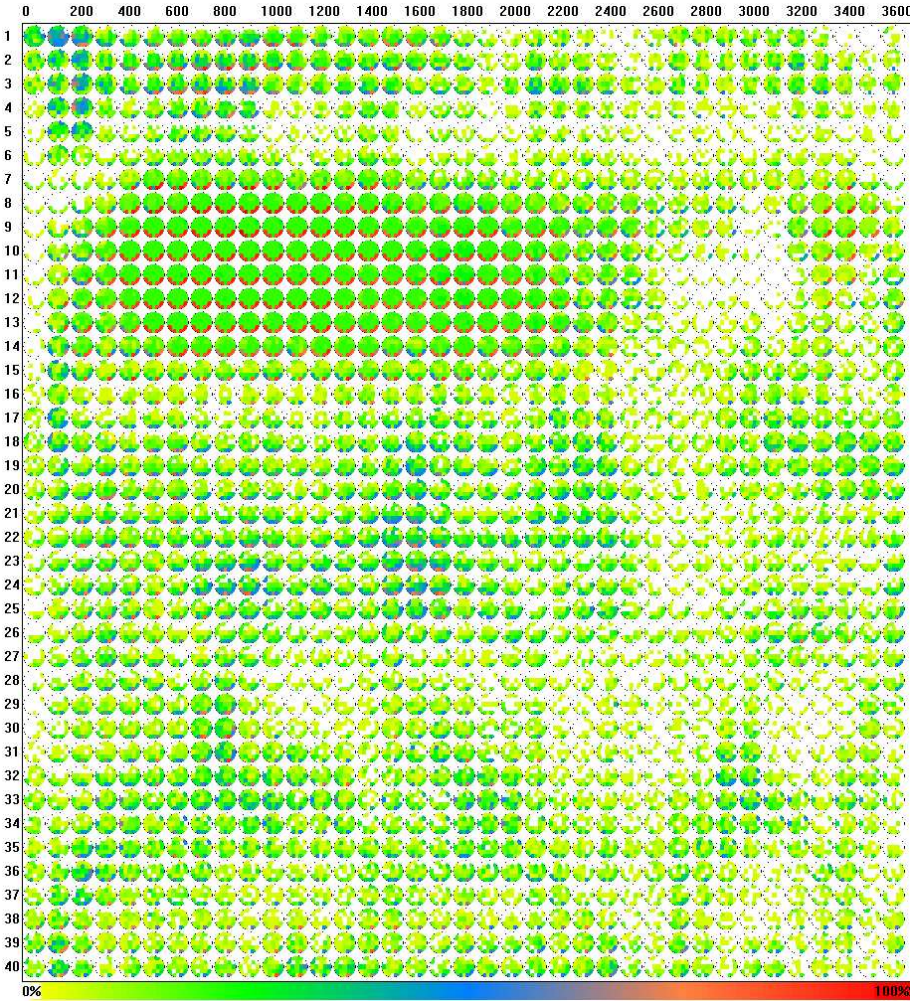

Figure 28: Full synchrony increase histogram for the 3-digit Sternberg experiment.

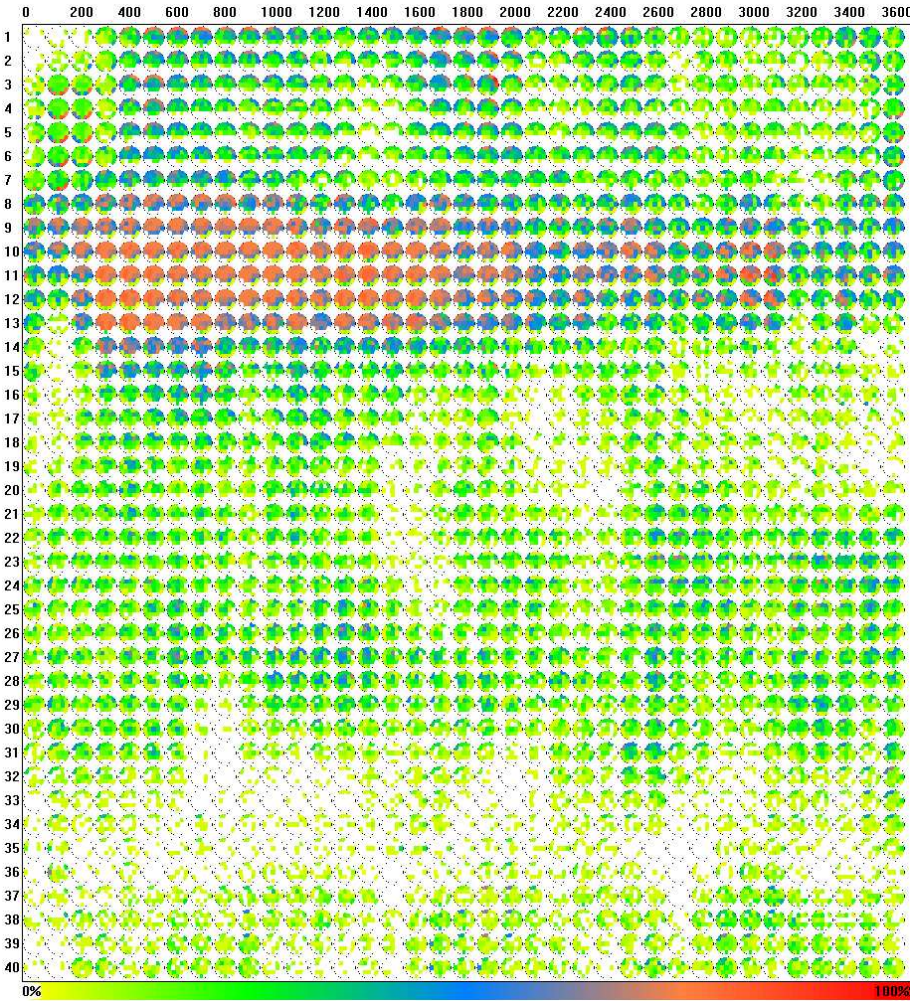

Figure 29: Full synchrony decrease histogram for the 3-digit Sternberg experiment.

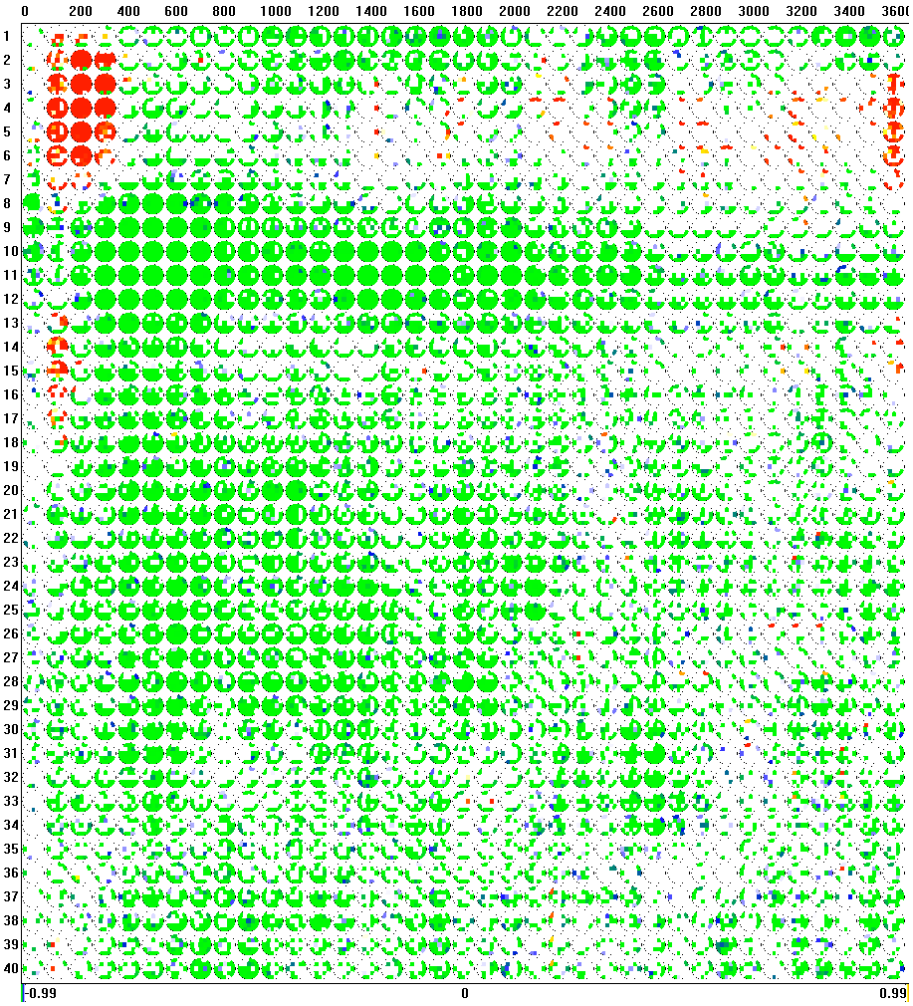

Figure 30: Map of significant amplitude changes for the 3-digit Sternberg experiment.

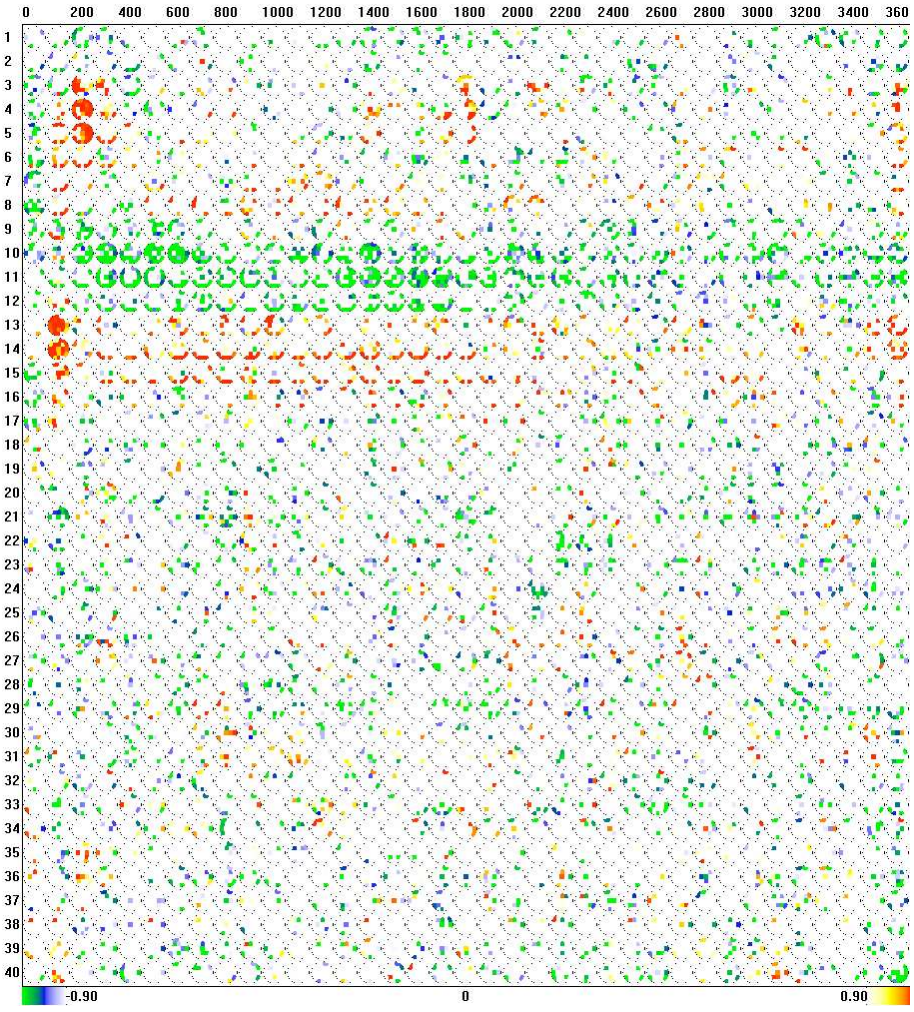

Figure 31: Map of significant LPD changes for the 3-digit Sternberg experiment.

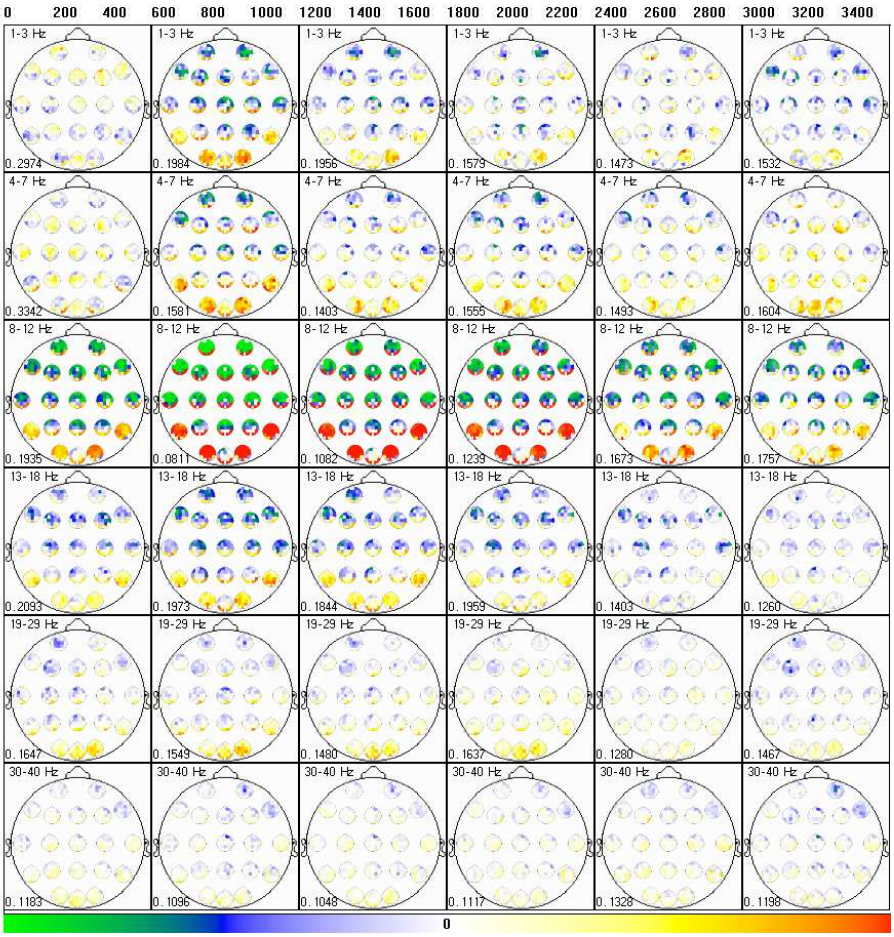

Figure 32: Full automatic segmentation for the 5-digit Sternberg experiment.

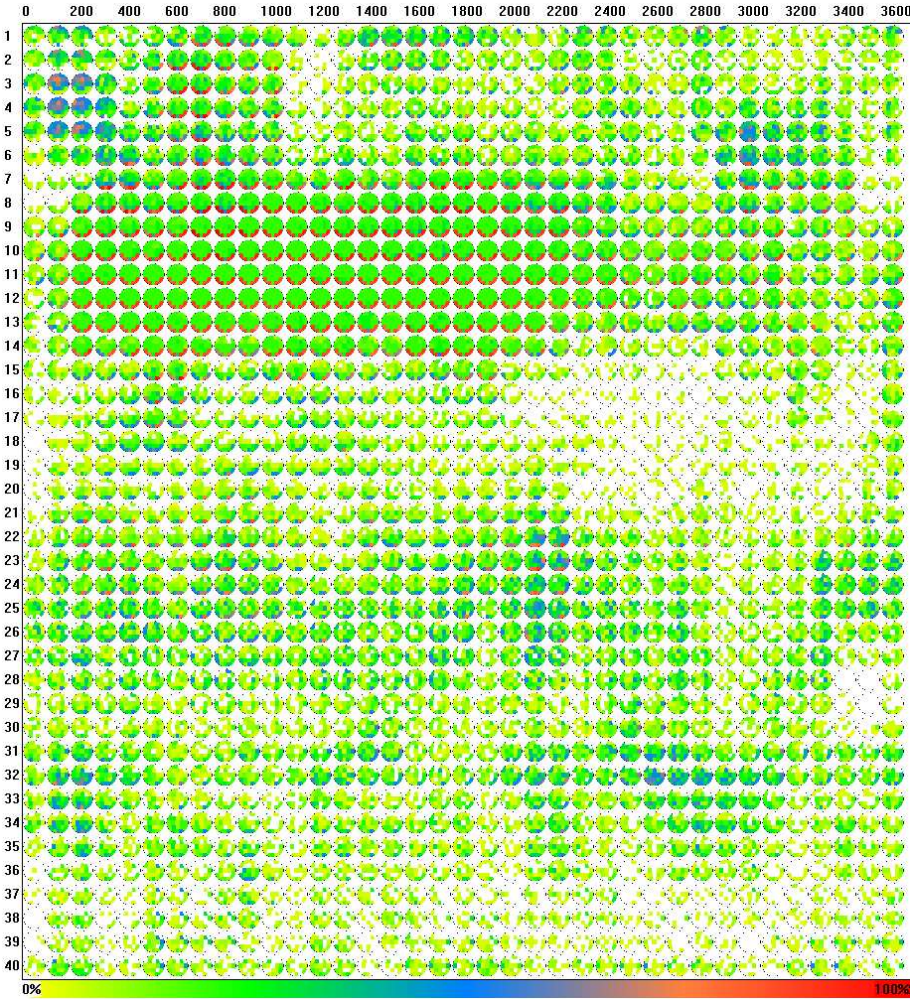

Figure 33: Full synchrony increase histogram for the 5-digit Sternberg experiment.

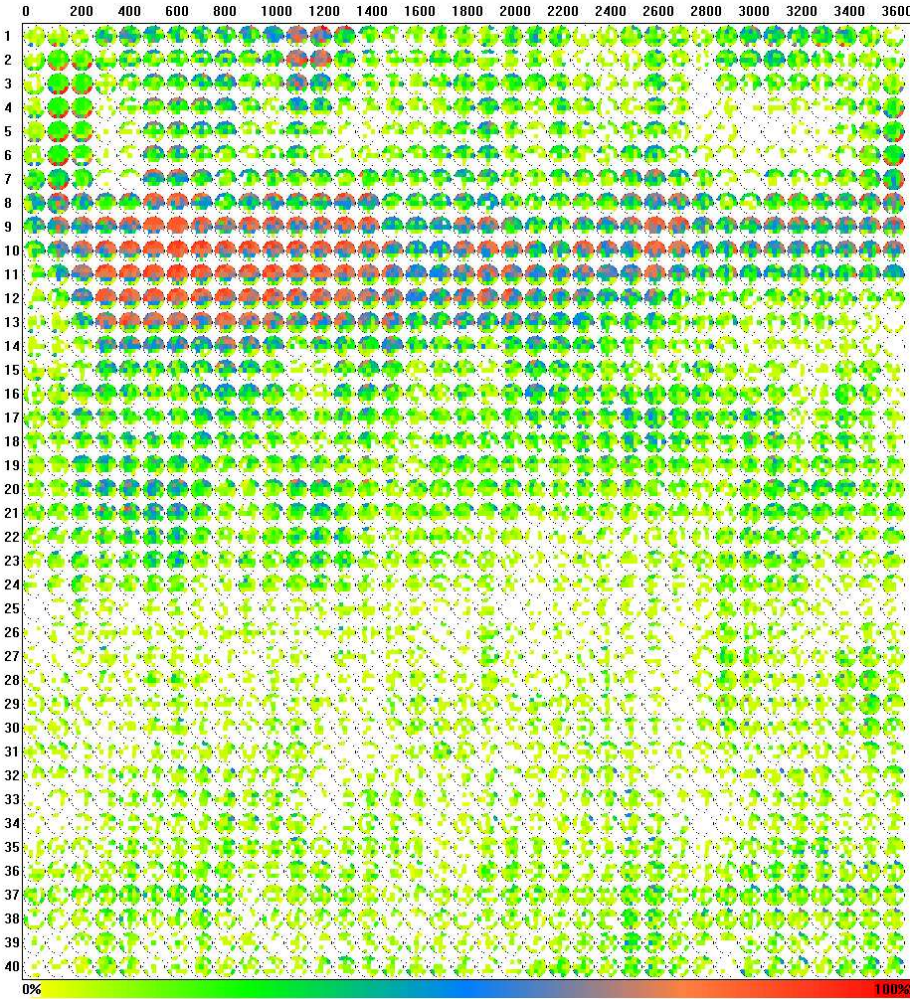

Figure 34: Full synchrony decrease histogram for the 5-digit Sternberg experiment.

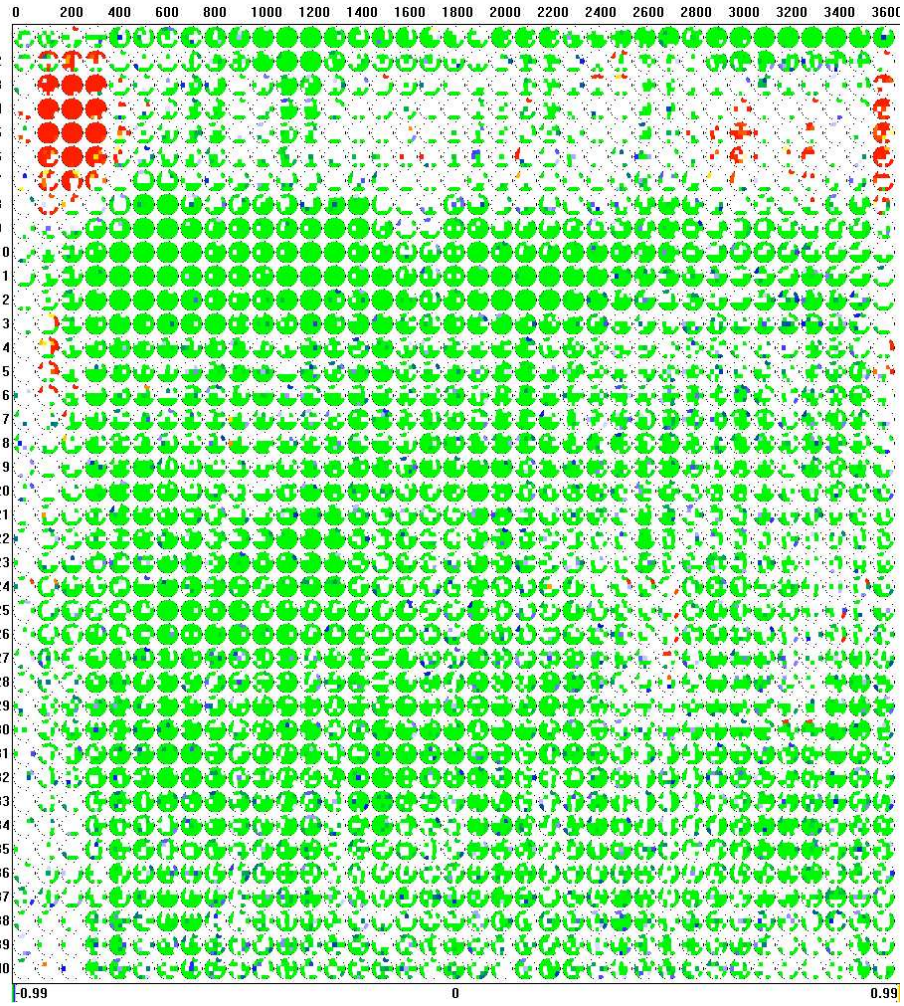

Figure 35: Map of significant amplitude changes for the 5-digit Sternberg experiment.

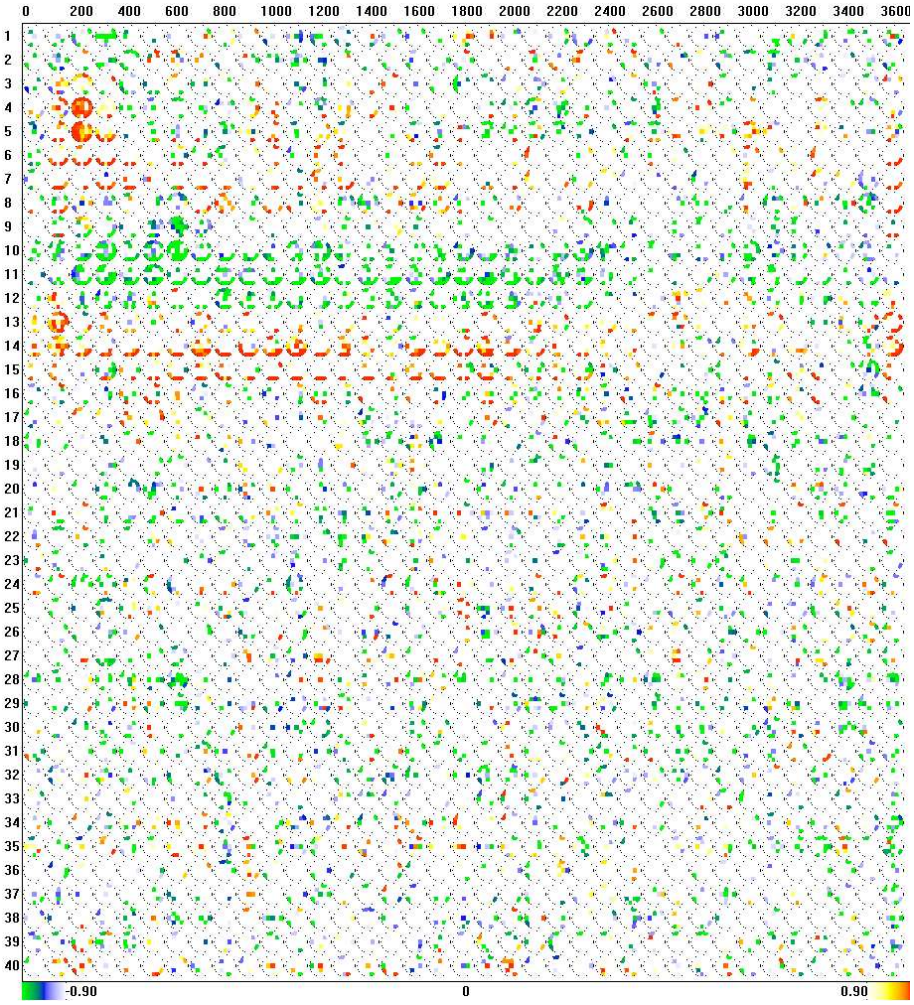

Figure 36: Map of significant LPD changes for the 5-digit Sternberg experiment.

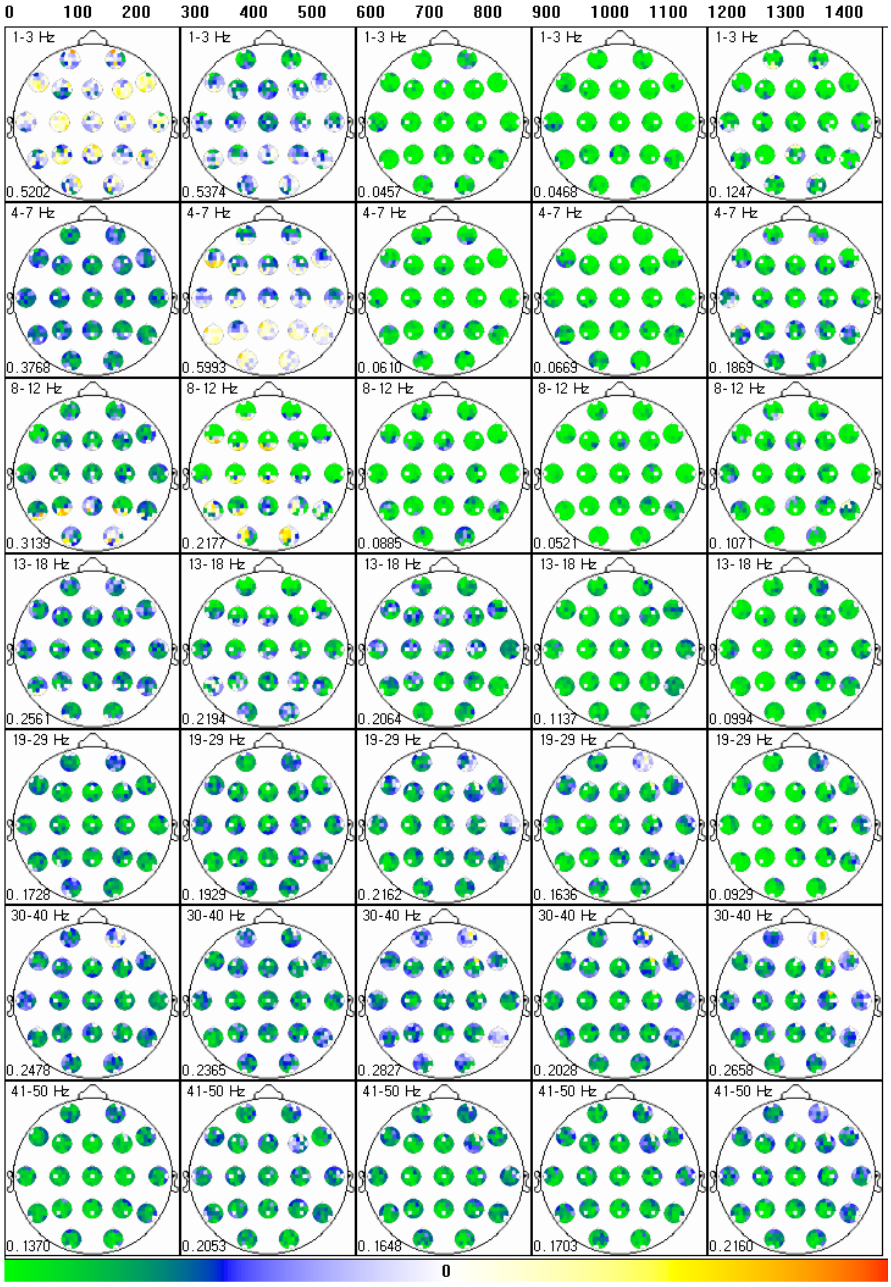

Figure 37: Full automatic segmentation for the Letters (Go condition) experiment.

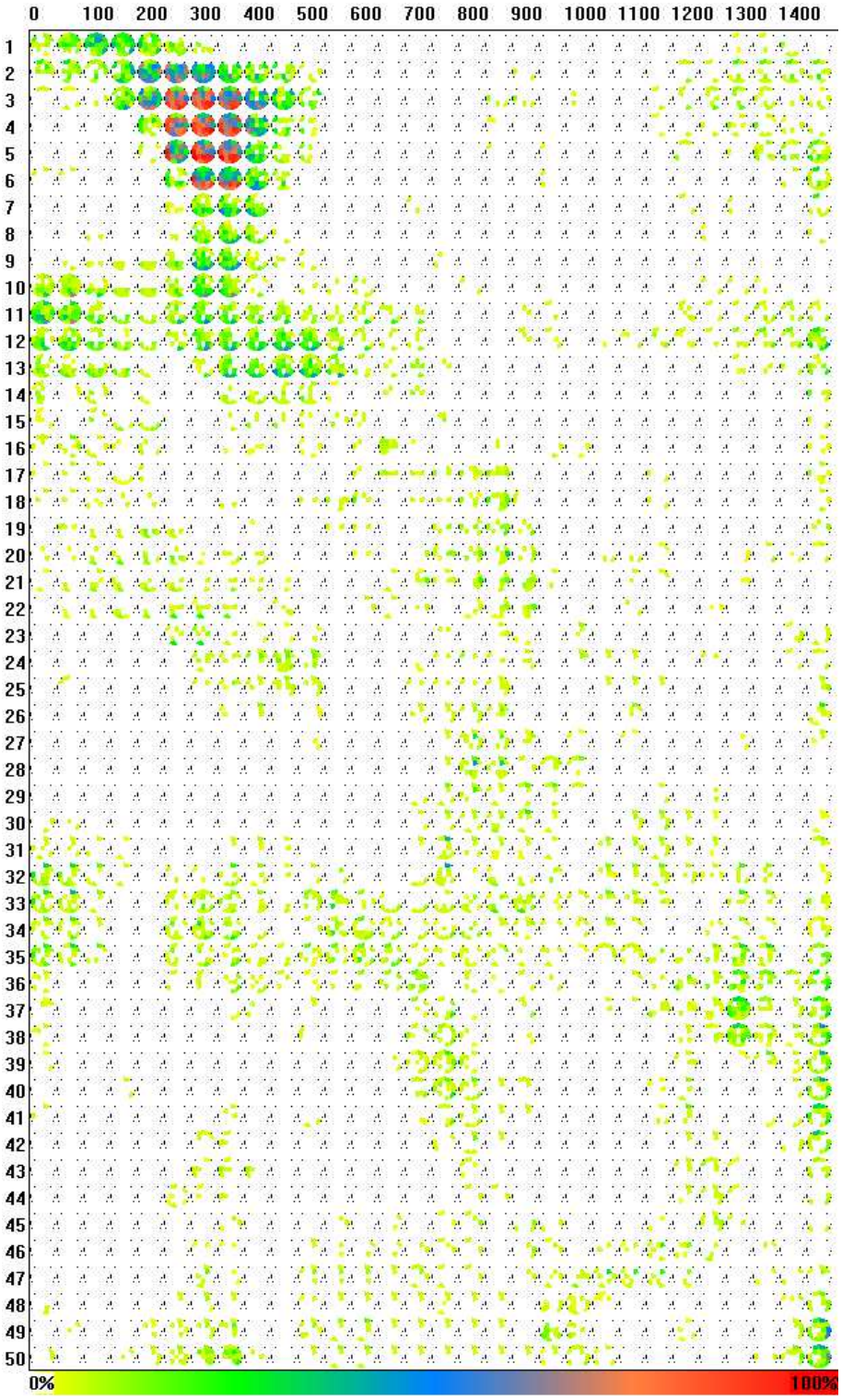

Figure 38: Full synchrony increase histogram for the Letters (Go condition) experiment.

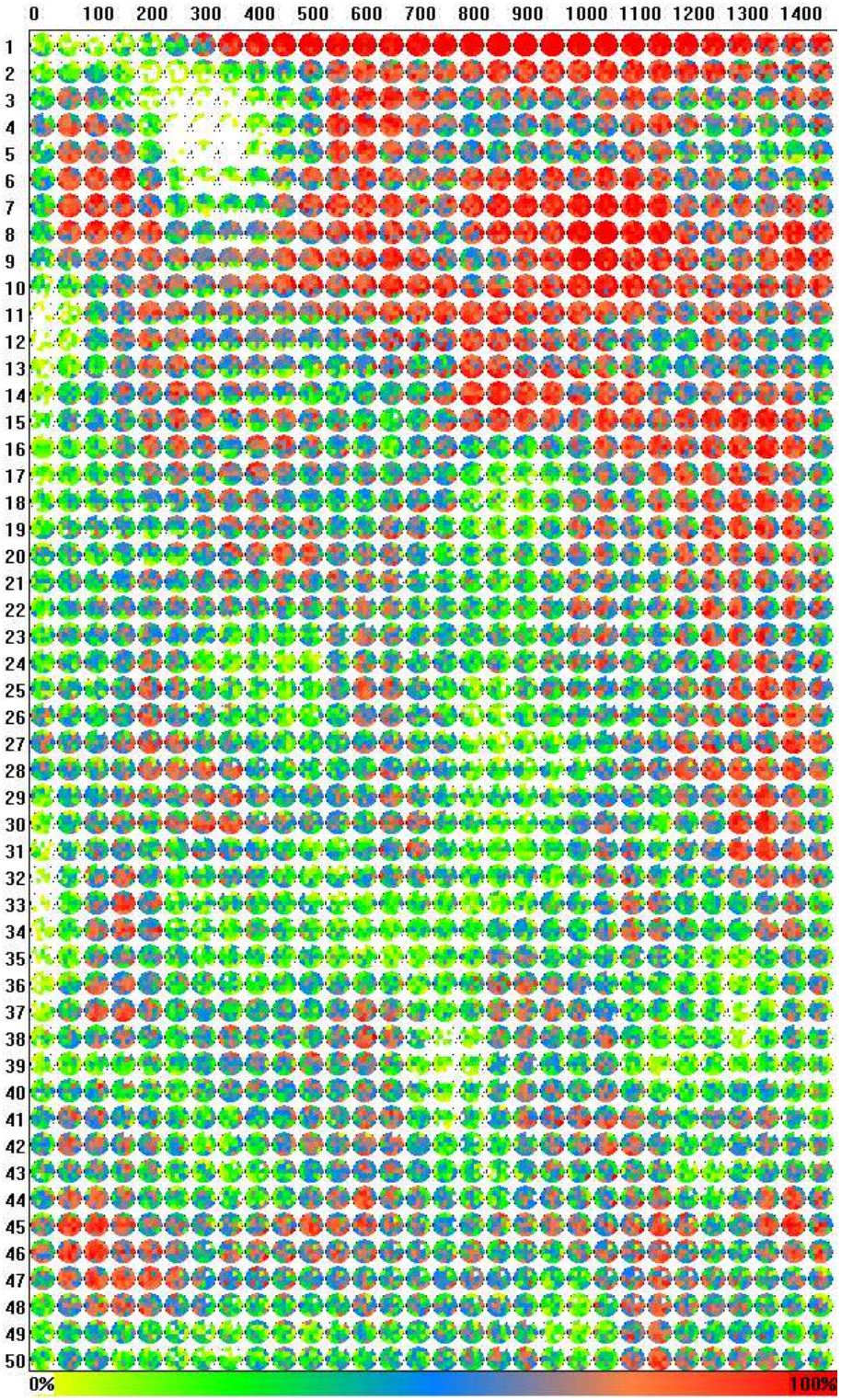

Figure 39: Full synchrony decrease histogram for the Letters (Go condition) experiment.

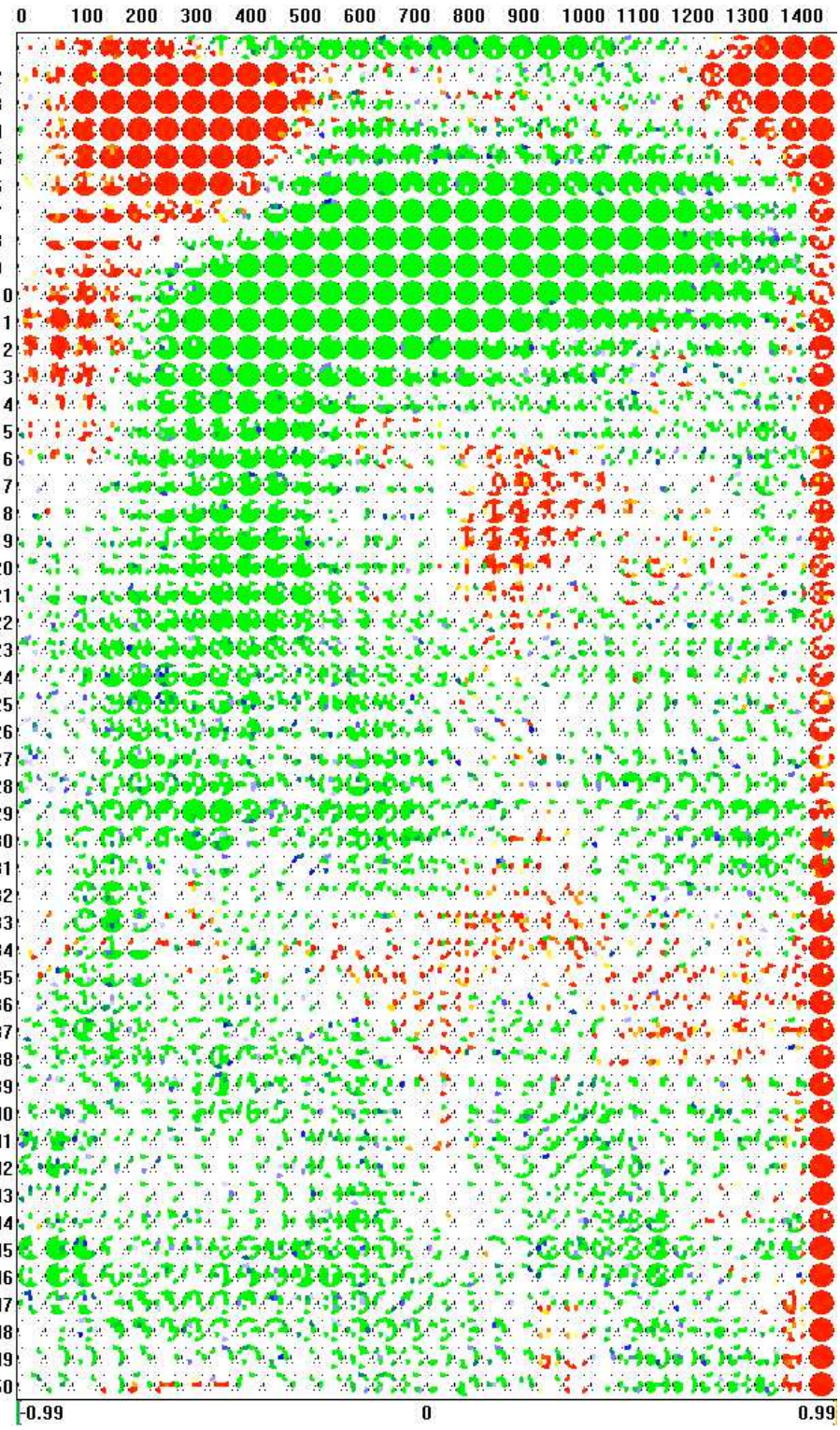

Figure 40: Map of significant amplitude changes for the Letters (Go condition) experiment.

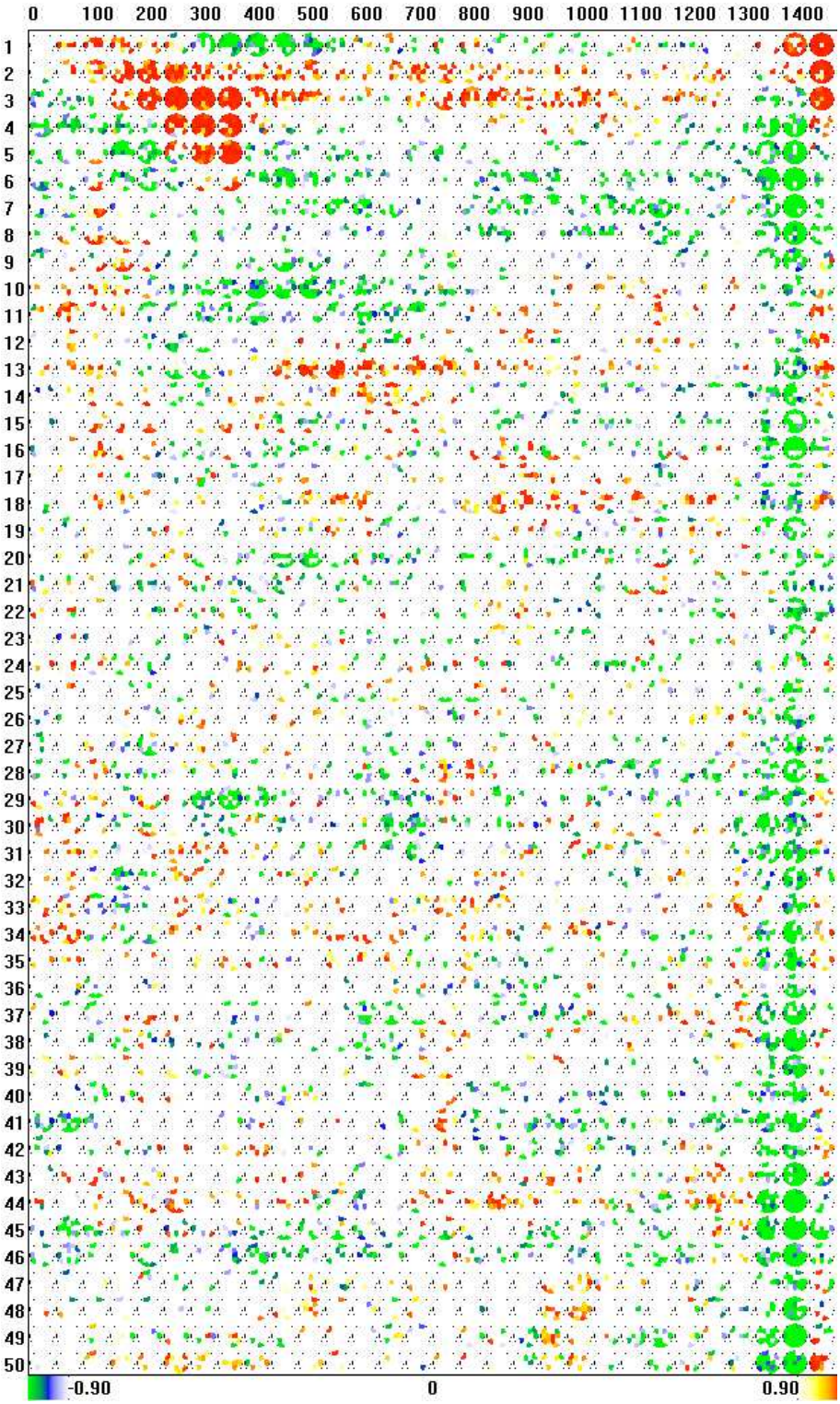

Figure 41: Map of significant LPD changes for the Letters (Go condition) experiment.

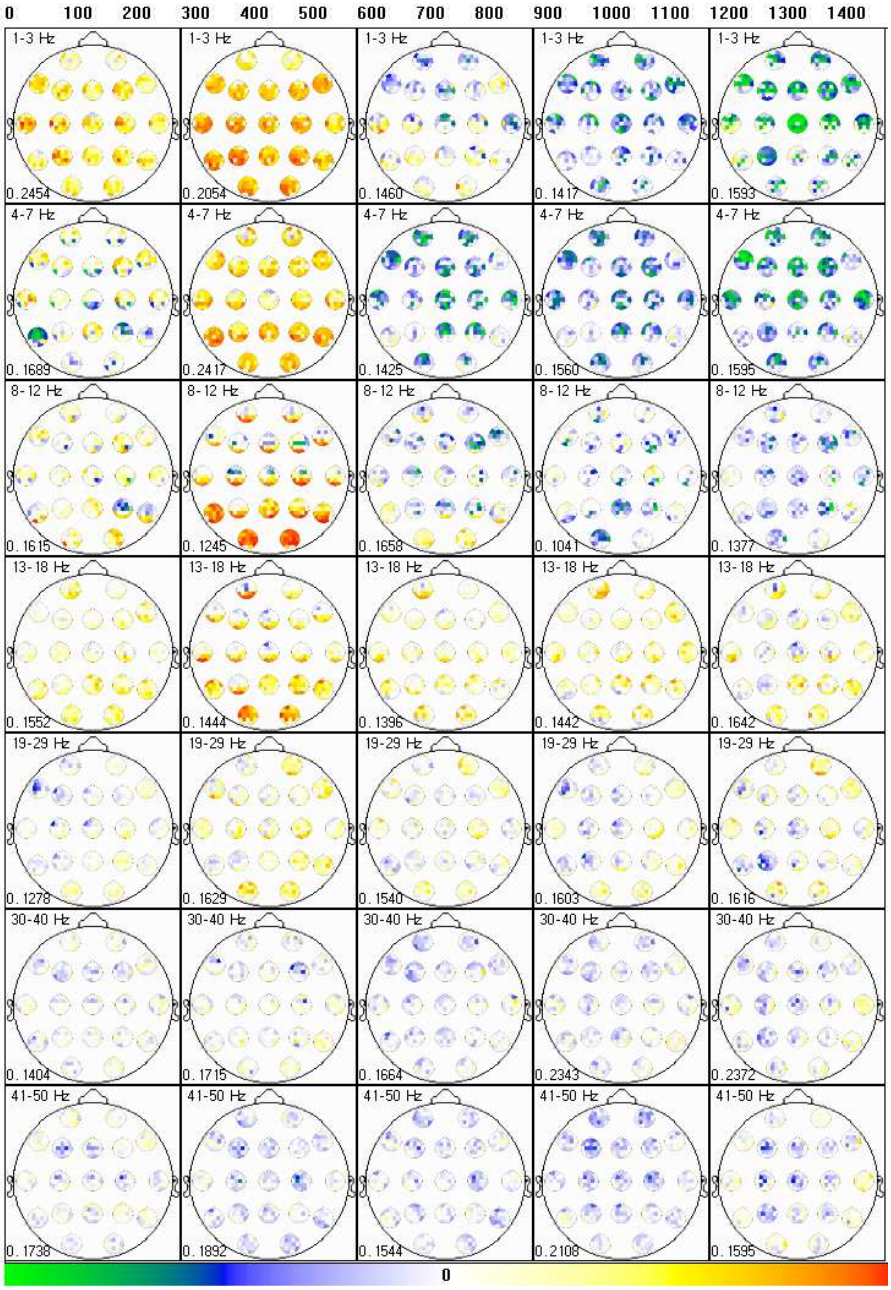

Figure 42: Full automatic segmentation for the Letters (NoGo condition) experiment.

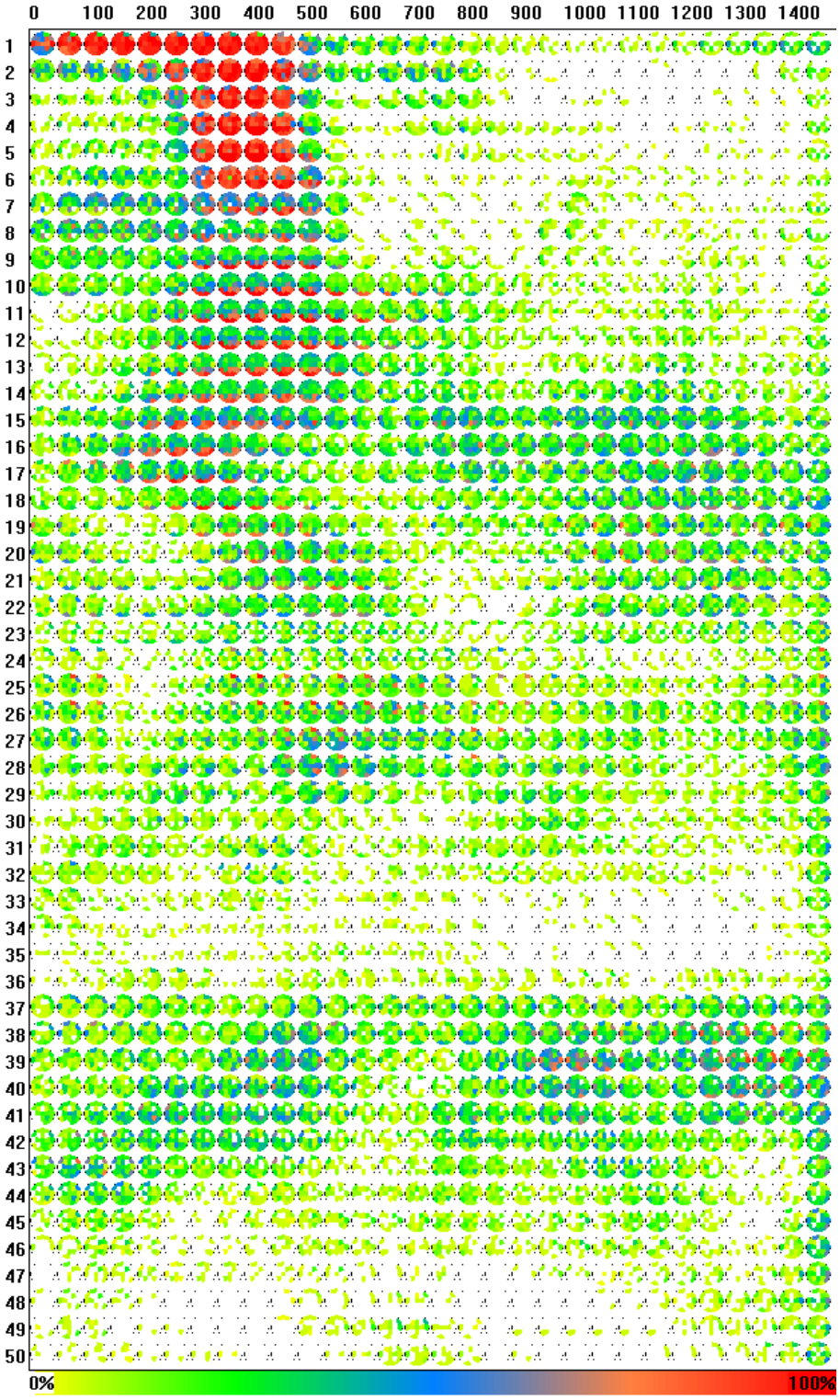

Figure 43: Full synchrony increase histogram for the Letters (NoGo condition) experiment.

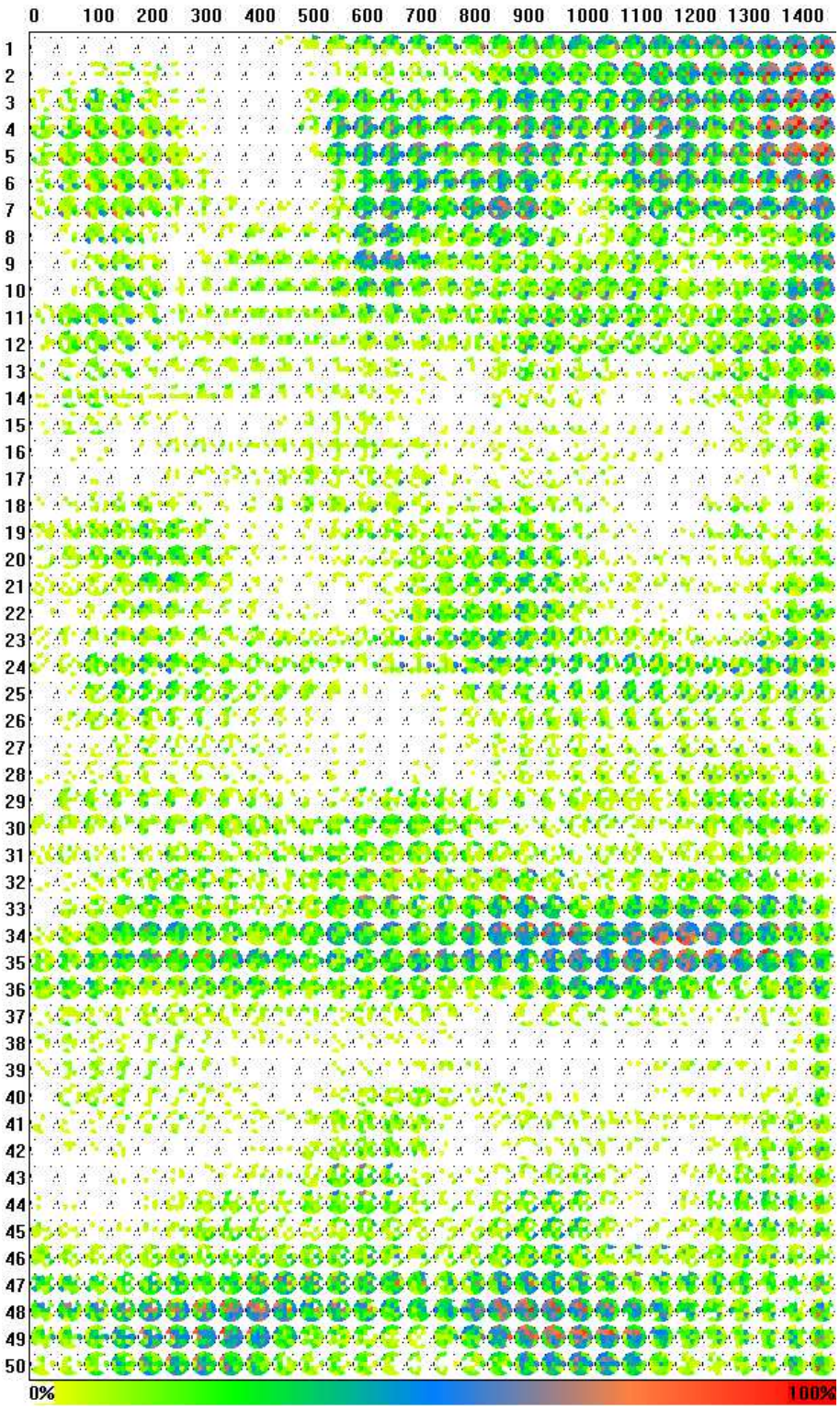

Figure 44: Full synchrony decrease histogram for the Letters (NoGo condition) experiment.

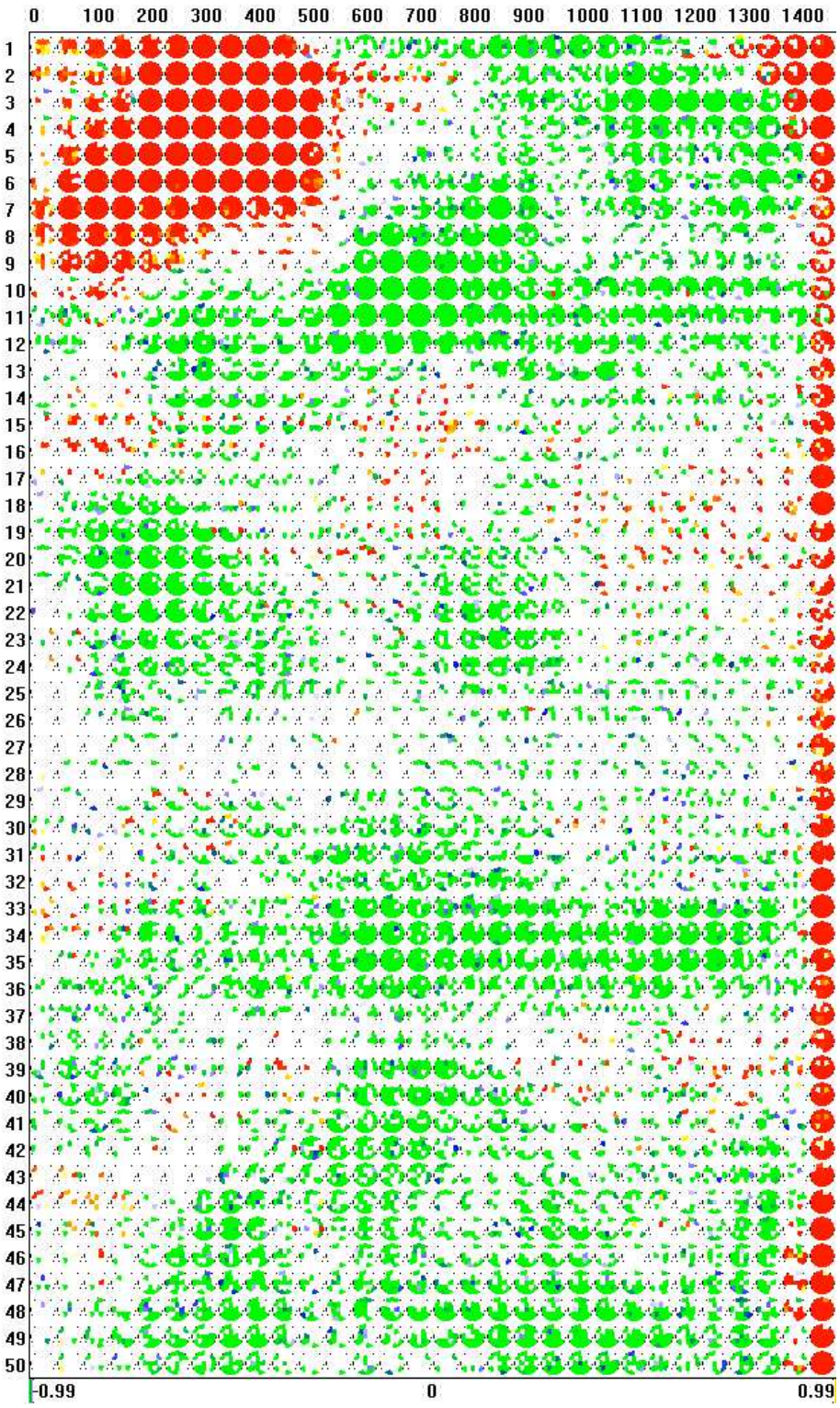

Figure 45: Map of significant amplitude changes for the Letters (NoGo condition) experiment.

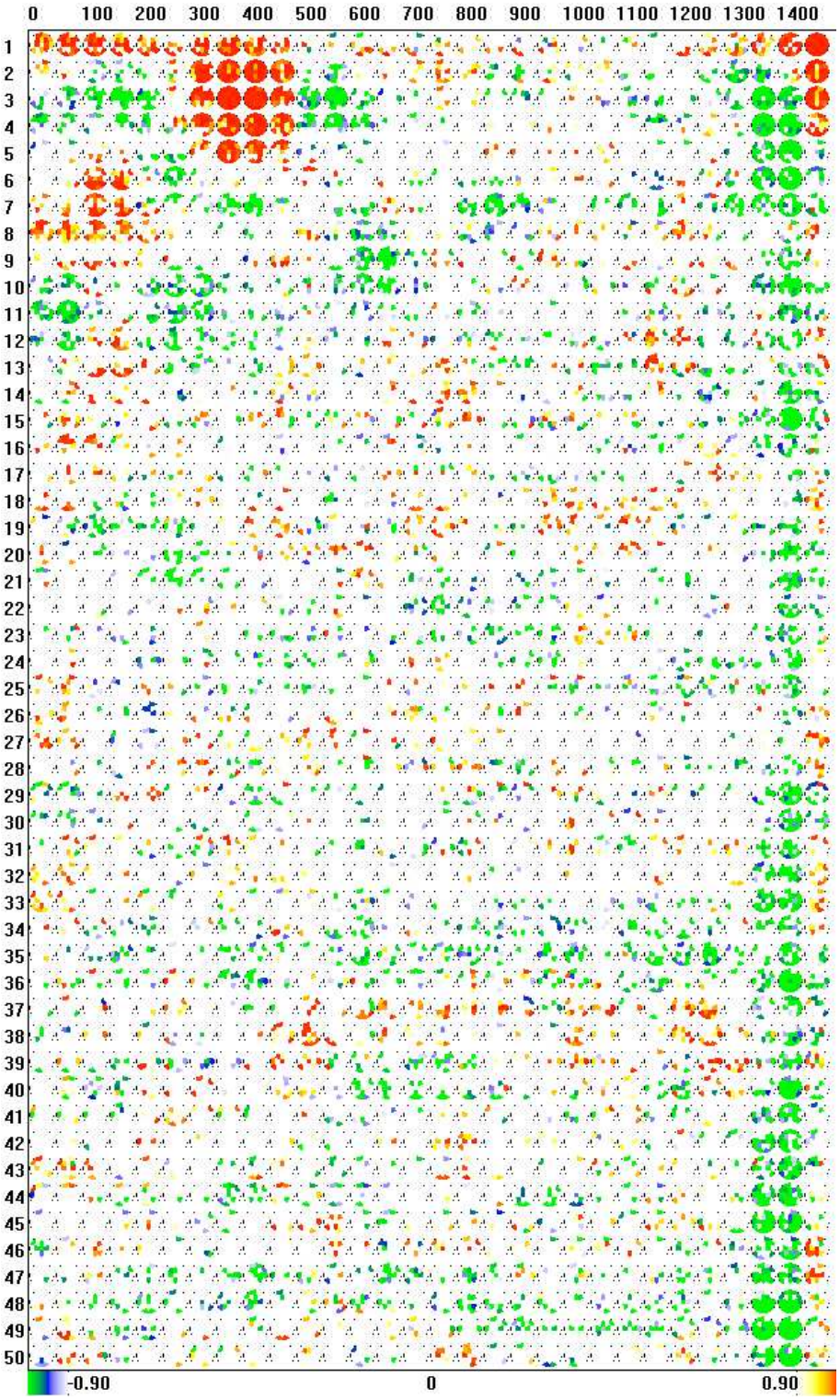

Figure 46: Map of significant LPD changes for the Letters (NoGo condition) experiment.

References

[1] Barde, L.H., Thompson-Schill S.L., 2002. Models of functional organization of the lateral prefrontal cortex in verbal working memory: Evidence in favor of the process model. J Cogn Neurosci. 14: 1054-1063.

[2] Bastiaansen, M., Hagoort, P., 2003. Event-induced theta responses as a window of the dynamics of memory. Cortex. 39: 967-992.

[3] Bressler, S.L., Coppola, R., Nakamura, R., 1993. Episodic multiregional cortical coherence at multiple frequencies during visual task performance. Nature. 366: 153-156.

[4] Bressler, S.L., 1995. Large-scale cortical networks and cognition. Brain Research Reviews. 20: 288-304.

[5] David, O., Garnero, L., Varela, F.J., 2001. A New Approach to the MEG/EEG Inverse Problem for the Recovery of Cortical Phase-Synchrony. IMPI 2001: 272-285.

[6] David, O. Friston, K.J., 2003. A neural mass model for MEG/EEG coupling and neuronal dynamics. NeuroImage. 20: 1743-1755.

[7] David, O., Cosmelli, D., Friston, K.J., 2004. Evaluation of different measures of functional connectivity using a neural mass model. NeuroImage. 21: 659-673.

[8] Fisher, N.I., 1995. Statistical Analysis of Circular Data. Cambridge University Press.

[9] Foxe J.J., McCourt M.E., Javitt D.C., 2003. Right hemisphere control of visuospatial attention: line-bisection judgements evaluated with high-density electrical mapping and source analysis. Neuroimage. 19: 710-726.

[10] Friston, K.J., Stephan, K.M.,Frackowiak, R.S.J., 1997. Transient Phase-Locking and Dynamic Correlations: Are They the Same Thing?. Human Brain Mapping. 5: 48-57.

[11] Gardner, W.A., 1992. A unifying view of coherence in signal processing. Signal Processing. 29: 113-140. Elsevier.

[12] Gevins, A., Smith, M., McEvoy, L., Yu, D., 1997. High-resolution EEG mapping of cortical activation related to working memory: effects opf task difficulty, type of processing, and practice. Cereb Cortex. 7: 374-385.

[13] Gross, J., Kujala, J., Hamalainen, M., Timmermann, L., Schnitzler, A., Salmelin, R., 2001. Dynamic imaging of coherent sources: Studying neural interactions in the human brain. PNAS. Vol. 98, No. 2: 694-699.

[14] Guerrero, J.A., Marroquin, J.L., Rivera, M., Quiroga, J.A., 2005. Adaptive monogenic filtering and normalization of ESPI fringe patterns. Opt Lett. 30, 22: 3018-3020.

[15] Hagemann, D., Naumann, E., Thayer, J.F., 2001. The quest for the EEG reference revisited: A glance from brain asmmetry researh. Psychophysiology. 38: 847-857. Cambridge University Press.

[16] Harmony, T., Fernandez, T., Fernandez-Bouzas, A., Silva-Pereyra, J., Bosch, J., Diaz-Comas, L., Galan, L., 2001. EEG changes during word and figure categorization. Clin. Neurophys. 112: 1486-1498.

[17] Harmony, T., Fernandez, T., Gersenowies, J., Galan, L., Fernandez-Bouzas, A., Aubert, E., Diaz-Comas, L., 2004. Specific EEG frequencies signal general common cognitive processes as well as specific task processes in man. International Journal of Psychophysiology. 53: 207-216.

[18] Hebb DO, 1949. The organization of behaviour. Wiley, New York.

[19] Hjorth B., 1975. An On-Line Transformation of EEG Scalp Potentials Into Orthogonal Source Derivations. Electroencephalography and Clinical Neurophysiology. 39: 526-530. Elsevier.

[20] Hoechstetter K., Bornfleth H., Weckesser D., Ille N., Berg P., Scherg M., 2004. BESA Source Coherence: A New Method to Study Cortical Oscillatory Coupling. Brain Topogr. 16(4): 233-238.

[21] Jimenez, J.C., Biscay, R., Montoto, O., 1995. Modeling the electroencephalogram by means of spatial spline smoothing and temporal autoregression. Biol. Cybern. 72: 249-259.

[22] Kirschfeld K., 2005. The physical basis of alpha waves in the electroencephalogram and the origin of the "Berger effect". Biol Cybern. 92: 177-185.

[23] Klimesch, W., 1999. EEG alpha and theta oscillations reflect cognitive and memory performance: a review and analysis. Brain Res Rev. 29: 169-195.

[24] Klimesch, W., Schack, B., Schabus, M., Doppelmayr, M., Gruber, W., Sauseng, P., 2004. Phase-locked alpha and theta oscillations generate the P1-N1 complex and are related to memory performance. Cogn Brain Res, 19: 302-316.

[25] Lachaux, J.P., Rodriguez, E., Martinerie, J., Varela, F.J., 1999. Measuring Phase Synchrony in Brain Signals. Human Brain Mapping. 8: 194-208.

[26] Lachaux, J.P., Rodriguez, E., Le Van Quyen, M., Martinerie, J., Varela, F.J., 2000. Studying single-trials of phase-synchronous activity in the brain. Int J Bifur Chaos. 10: 2429-2439.

[27] Law, S.K., Nunez, P.L., Wijesinghe, R.S., 1993. IEEE Transactions on Biomedical Engineering. Vol. 40, No. 2: 145-153.

[28] Lopes da Silva F.H., 1991. Neural mechanisms underlying brain waves: from neural membranes to networks. Electroenceph. Clin Neurophysiol. 79: 81-93.

[29] Luria, A.R., 1966. Higher Cortical Functions in Man. Basic Books, New York.

[30] Malmivuo, J., Plonsey, R., 1995. Bioelectromagnetism: Principles and Applications of Bioelectric and Biomagnetic Fields. Oxford University Press.

[31] Marroquin, J.L., Mitter, S., Poggio, T., 1987. Probabilistic Solution of Ill-Posed Problems in Computational Vision. J. Am. Stat. Assoc. 82: 76-89.

[32] Marroquin, J.L., Figueroa, J.E., 1997. Robust quadrature filters. J. Opt. Soc. Am. Vol. 14, No. 4: 779-791.

[33] Marroquin, J.L., Velasco, F.A., Rivera, M., Nakamura, M., 2001. Gauss-Markov Measure Field Models for Low-Level Vision. IEEE Transactions on Pattern Analysis and Machine Intelligence. Vol. 23. No. 4: 337-348.

[34] Marroquin, J.L., Harmony, T., Rodriguez, V., Valdes, P., 2004. Exploratory EEG data analysis for psychophysiological experiments. NeuroImage. 21: 991-999.

[35] Mizuhara, H., Wang, L., Kobayashi, K., Yamaguchi, Y., 2005. Long-range EEG phase synchronization during an arithmetic task indexes a coherent cortical network simultaneously measured by fMRI. NeuroImage. Vol. 27, No. 3: 553-563.

[36] Neuper, C., Grabner, R.H., Fink, A., Neubauer, A.C., 2005. Long term stability and consistency of EEG event-related (de-)syncronization across different cognitive tasks. Clin Neurophysiol, 116: 1681-1694.

[37] Nunez, P.L., 1995. Neocortical Dynamics and Human EEG Rhythms. Oxford University Press.

[38] Pascual-Marqui, R.D., Gonzalez-Andino, S.L., Valdes-Sosa, P.A., Biscay-Lirio, R., 1988. Current Source Density Estimation and Interpolation Based on the Spherical Harmonic Fourier Expansion. Int J Neurosci. 43(3-4): 237-249.

[39] Perrin, F., Pernier, J., Bertrand, O., Echallier, J.F., 1989. Spherical splines for scalp potential and current density mapping. Electroencephalography and clinical Neurophysiology. 72, 184-187. Elsevier Scientific Publishers, Ltd.

[40] Pfurtscheller, G., 1977. Graphical display and statistical evaluation of event-related desynchronization (ERD). Electroenceph clin Neurophysiol. 43: 757-760.

[41] Pfurtscheller, G., 1992. Event-related synchronization: an electrophysiological correlate of cortical areas at rest. Electroenceph clin Neurophysiol. 83: 62-69.

[42] Pfurtscheller, G., Lopes da Silva F.H., 1999. Event-related EEG/MEG synchronization and desynchronization: basic principles. Clinical Neurophysiology. 110: 1842-1857.

[43] Quian Quiroga, R., Kraskov, A., Kreuz, T., Grassberger, P., 2002. Performance of different synchronization measures in real data: A case study on electroencephalographic signals. Physical Review E. 65, 041903.

[44] Rhom, D., Klimesch, W., Haider, H., Doppelmayr, M., 2001. The role of theta and alpha oscillations for language comprehension in the human electroencephalogram. Neurosci Lett. 310: 137.140.

[45] Rodriguez, E., George, N., Lachaux, J.P., Martinerie, J., Renault, B., Varela, F.J., 1999. Perception's shadow: long-distance synchronization of human brain activity. Nature. 397: 430-433.

[46] Sarnthein, J., Petsche, H., Rappelsberger, P., Shaw, G.L., Von Stein, A., 1998. Synchronization between prefrontal and posterior association cortex during human working memory. Proc Natl Acad Sci USA. 95: 7092-7096.

[47] Silverman, B.W., 1986. Density Estimation for Statistics and Data Analysis. Chapman and Hall, London.

[48] Singer W., 1993. Synchronization of cortical activity and its outative role in information processing and learning. Ann Rev Physiol. 55: 349-374.

[49] Tallon-Baudry, C., Bertrand, O., Delpuech, C., Pernier, J., 1997. Oscillatory g-Band (30-70 Hz) activity induced by a visual task in humans. J Neuroscience. 15: 722-734.

[50] Tallon-Baudry, C., Bertrand, O., Fisher, C., 2001. Oscillatory synchrony between human extrastriate areas during visual short-term memory maintenance. J Neurosci. 15, RC177.

[51] Ungerleider, L.G., Courtney, S.M., Haxby, J.V., 1998. A neural system for human visual working memory. Proc Natl Acad Sci USA. 95: 883-890.

[52] Varela, F.J., Lachaux, J.P., Rodriguez, E., Martinerie, J., 2001. The Brainweb: Phase Synchronization and Large-Scale Integration. Nature Reviews, Neuroscience. 2: 229-239.

[53] Yao D., 2002. The theoretical relation of scalp Laplacian and scalp current density of spherical shell head model. Phys. Med. Biol. 47: 2179-2185.

[54] Zhang, Z., 1995. A fast method to compute surface potentials generated by dipoles within multilayer anisotropic spheres. Phys. Med. Biol. 40: 335-349.